10-11-2019

Finite Element Modelling And Analysis Of Rc Beams Strengthened For Flexure Using BFRP Fabrics

Iyinoluwa Stephen
University of Windsor

FINITE ELEMENT MODELLING AND ANALYSIS OF RC BEAMS STRENGTHENED FOR FLEXURE USING BFRP FABRICS

By

Iyinoluwa Stephen

A Thesis
Submitted to the Faculty of Graduate Studies
through the Department of Civil and Environmental Engineering
in Partial Fulfillment of the Requirements for
the Degree of Master of Applied Science
at the University of Windsor

Windsor, Ontario, Canada

2019

FINITE ELEMENT MODELLING AND ANALYSIS OF RC BEAMS STRENGTHENED FOR FLEXURE USING BFRP FABRICS

by

Iyinoluwa Stephen

APPROVED BY:

_____

N. Zamani
Departmental of Mechanical, Automotive and Materials Engineering

_____

S. Kenno
Department of Civil and Environmental Engineering

_____

S. Das, Advisor
Department of Civil and Environmental Engineering

October 8, 2019

DECLARATION OF ORIGINALITY

I hereby certify that I am the sole author of this thesis and that no part of this thesis has been published or submitted for publication. However, the results of this thesis were validated with the experimental work done conducted Mr. Eric Hughes.

I certify that, to the best of my knowledge, my thesis does not infringe upon anyone's copyright nor violate any proprietary rights and that any ideas, techniques, quotations, or any other material from the work of other people included in my thesis, published or otherwise, are fully acknowledged in accordance with the standard referencing practices. Furthermore, to the extent that I have included copyrighted material that surpasses the bounds of fair dealing within the meaning of the Canada Copyright Act, I certify that I have obtained a written permission from the copyright owner(s) to include such material(s) in my thesis and have included copies of such copyright clearances to my appendix.

I declare that this is a true copy of my thesis, including any final revisions, as approved by my thesis committee and the Graduate Studies office, and that this thesis has not been submitted for a higher degree to any other University or Institution.

ABSTRACT

The increasing cost of new infrastructure in addition to the gradual decline in the structural integrity of current aging infrastructure has necessitated studies for sustainable materials for strengthening concrete structures. Extensive experimental and numerical studies using carbon fiber reinforced polymers (CFRP) and glass fiber reinforced polymers (GFRP) for strengthening concrete structures have concluded on their immense efficiency in increasing the ultimate capacity of such structures. Basalt fiber reinforced polymer (BFRP), however, is a relatively new material in the construction industry with limited experimental and numerical studies. This study presents a non-linear numerical analysis on reinforced concrete beams strengthened with basalt fiber reinforced polymer (BFRP) fabrics using finite element (FE) software, Abaqus. The load-deflection behavior, failure modes, ductility index and cracking patterns of the beams were analysed and compared to experimental results obtained from literature. The FE model was observed to have a good correlation with the test results and was able to predict the elastic and plastic behavior of the concrete beams. The results of the FE analysis indicate that BFRP fabrics were able to increase the load capacity of the strengthened beams up to 120% and the ductility up to 67% over the control beam. However, the strengthening scheme must remain within the optimum number of layers to ensure that the beams do not experience sudden and brittle failure.

DEDICATION

I would like to dedicate this to God and my Lord and Saviour Jesus Christ for His wisdom and grace to start and complete this project.

To my family for their love and support and to my lovely fiancé for her patience and understanding.

ACKNOWLEDGEMENTS

My profound gratitude goes to Dr Das for the opportunity to undertake my master's research under his supervision. Your continuous guidance and suggestions were invaluable throughout this project. I would also like to thank my committee members: Dr. Kenno and Dr. Zamani for their help and adept suggestions.

I am grateful for the support of our lab technicians, Matt St. Louis and Jerome Finnerty for their time and efforts during the preparation and testing of the specimen.

Finally, I want to specially thank Karla Gorospe and Eric Hughes and all my colleagues Jamshid Zohreh Heydariha, Jothiarun Dhanapal, Emad Booya, Soham Mitra, Amirezza Bastani, Sachith Jayasuriya, Jeeric Penales, Navjot Singh, Habeeb Sobanke and Adeyemi Adeshina for their help with the laborious tasks of specimen preparation and testing. This thesis would not have been completed without the support of these people.

TABLE OF CONTENTS

LIST OF TABLES

LIST OF FIGURES

Chapter 1

Chapter 2

Chapter 3

LIST OF ABBREVIATIONS

FRP – Fiber Reinforced Polymer

CFRP – Carbon Fiber Reinforced Polymer

GFRP – Glass Fiber Reinforced Polymer

BFRP – Basalt Fiber Reinforced Polymer

GNFRP – Green Natural Fiber Reinforced Polymer

DTT - Direct Tensile Test

WST – Wedge Splitting Test

TPB – Three Point Bending Test

CMOD – Crack Mouth Opening Displacement

CHAPTER 1
INTRODUCTION

1.1 General

One of the most widely used material in the construction industry today is concrete. Its versatility, strength, and cost-effectiveness are the major reasons for the multiplicity of its applications in the construction industry which range from buildings to highways, bridges as well as massive retaining structures such as dams. Despite its several advantages, concrete experiences major problems when subjected to tensile forces. Concrete tensile capacity is about 10% of its compressive strength thus presenting the need for tensile reinforcements. The use of steel rebar as tensile reinforcement for concrete has been adopted around the world due to its propitious properties of high modulus of elasticity, high ultimate tensile strain, and high tensile strength. Although reinforced concrete fuses the advantages of both concrete and steel to form a strong composite material, it is also plagued by the weakness of the materials. Reinforced concrete structures experience deterioration due to several factors such aging, severe weather conditions, change in use, and corrosion. Corrosion occurs in reinforced concrete due to the oxidation of the steel rebars when it is exposed to air and atmospheric moisture. This is a major catalyst for the failure of reinforced concrete structures as the formation of rust reduces the tensile capacity of the steel and weakens the bond between the concrete and steel. As rust continues to spread in the steel, it causes it to expand to more than twice its original size thus, resulting in cracking and spalling of the concrete cover and ultimately the failure of the concrete structure. The 2017 ASCE infrastructure report card reveals that almost four in every ten bridges in the United States was structurally deficient in 2016 and although this number is reducing, a total of $123 billion will be required to clear the backlog for

bridge rehabilitation (American Society Of Civil Engineers (ASCE), 2017). The 2019 Canadian infrastructure report card (CIRC) also reports that about 40% of Canadian road and bridge infrastructures are in poor condition with a replacement value of about $50 billion CAD (CIRC, 2019). This huge cost of replacement, however, has led into studies on methods for strengthening existing infrastructure. Several methods have adopted the position of externally strengthening the structure to restore the capacity to its design capacity. Some of these methods include the use of externally bonded steel plates, concrete and steel jacketing, and external post tensioning (Saadatmanesh and Ehsani, 2007; ACI, 2017).

Externally bonded steel plates as shown in Figure 1.1 provide an efficient method of strengthening existing structures and improving their load bearing capacity. Though cost-effectiveness and ease of application are some of its advantages, the high risk of corrosion at the steel and epoxy interface make it a non-durable alternative (Saadatmanesh and Ehsani, 2007). Another method of reinforcing an existing structure is through the use of steel jacketing, where the steel plates act as straps as shown in the Figure 1.2. The straps are placed at the corners and edges of the structure and are attached through welding or the use of epoxy. Studies conducted by Alim et al. (2013) showed the use of concrete jacket increases the load capacity and stiffness of beams as well as increasing axial and shear strength of columns. Although the use of a jacket is cost-effective option when compared to the cost of a new construction, it is susceptible to corrosion, time-consuming, labour and equipment intensive, and it requires continuous maintenance. The major disadvantages of using external post-tensioning for

strengthening existing structures is the difficulty associated with the installation of tendons and anchorages and corrosion of tendons (Saadatmanesh and Ehsani, 2007).

Figure 1.1: RC beam strengthened with steel plates (Nie et al., 2010)

Figure 1.2: Steel Jacketing of columns and beams (Indiamart, 2019)

The demand for an alternative non-corrosive reinforcement has thus significantly increased in recent times, leading to several research studies being conducted to find both

materials with good mechanical and non-corrosive properties as well as better reinforcing techniques. Recent studies have showed the viability and applicability of the use of composite materials such as fiber reinforced polymers (FRP) to solve these challenges.

1.2 Fibre Reinforced Polymers

Fiber reinforced polymers (FRPs) have been in use in the aeronautical and automobile industries since 1950 but it only began to be considered for structural applications in 1970 (Intelligent Sensing for Innovative Solutions Canada, 2007). Its applications have increased in recent times due to more understanding of its favorable characteristics such high strength to weight ratio, ease of application, chemical and weather inertness, and non-corrosive properties (Einde et al, 2003). FRPs are made up of two materials namely: continuous fibers and polymer matrix. The fiber can be made from various materials such as carbon, glass, aramid and can be of various form such as rod and mesh-forms as shown in Figures 1.3 and 1.4 as well as fabrics or discrete fibers as shown in Figures 1.5 and 1.6.

1.2.1 Manufacturing process

There are four widely used processes adopted in the manufacturing of FRPs which are pultrusion, filament winding, resin transfer moulding and semi-automated manufacturing (Einde et al., 2003). The type of fibers, shape, volumetric ratio, matrix adhesion, as well as the manufacturing process adopted determines the material properties of the FRP. The fibers are attached together using a matrix that ensures that the fibers are protected from abrasion and the stresses are transferred effectively. Two types of matrices are used for this purpose namely: thermosetting and thermoplastic, with the thermosetting matrix being the most commonly used of the two options. This is because although a

thermoplastic matrix can be reshaped by reheating, the mechanical properties of the fibers are altered and reduced during the heating process. Thermosetting matrices have good thermal and chemical properties as they are connected by chemical crosslinks which form three dimensional structures that cannot be reshaped by reheating (Intelligent Sensing for Innovative Solutions Canada, 2007).

Figure 1.3: FRP rods

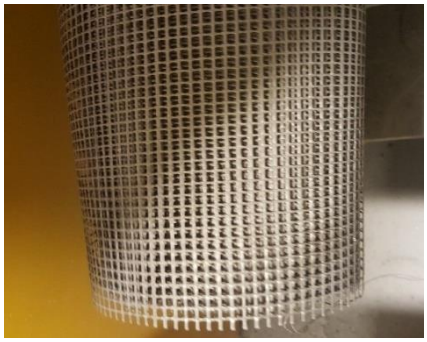

Figure 1.4: FRP mesh

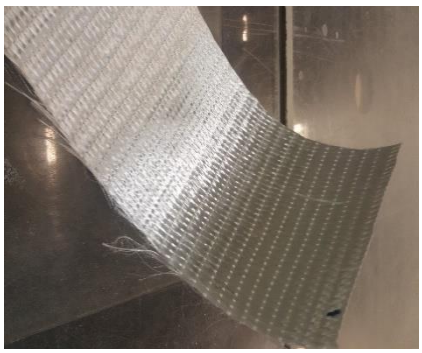

Figure 1.5: FRP Fabrics

Figure 1.6: FRP discrete fibers

1.2.2 Mechanical properties

The behavior of any strengthening scheme using FRPs is dependent on the mechanical properties of the individual fibers chosen. FRP are linear elastic materials and thus, the constitutive relation between stress and strain is governed by the elastic modulus. Carbon fiber reinforced polymer (CFRP) possesses a higher elastic modulus and tensile strength

compared to glass fiber reinforced polymer (GFRP), aramid fiber reinforced polymer (AFRP) and steel as shown in Table 1.1 below. This means that of the three fibers, CFRP can withstand higher loads and higher stresses which provides a great advantage over steel when strengthening existing concrete structures. However, the value of the ultimate strain is a vital parameter to be considered when reinforcing concrete in flexure as it is representative of how much deformation the fiber can be subjected to before its rupture. A higher value of ultimate strain is more desirable for a structure designed for flexure as a lower value can reverse the behavior and make it brittle. A brittle failure is sudden and unsafe and should be avoided at all cost during design or strengthening. As can be found from Table 1.1, CFRP exhibits the lowest deformability characteristics, which is a severe disadvantage when used for rehabilitation of a structure.

Table 1.1: Mechanical properties of FRP and steel reinforcement (Intelligent Sensing for Innovative Solutions, 2007)

Mechanical properties	Steel Rebars	CFRP fabric	GFRP fabric	AFRP fabric
Elastic modulus (GPa)	200	150-175	30-50	50-75
Tensile Strength (MPa)	400-500	1600-2400	500-1000	1200-2000
Ultimate strain (%)	~30	1.0-1.5	1.5-2.0	2.0-2.6

1.3 Basalt Fibers

Basalt is a naturally occurring igneous rock formed by the freezing of volcanic lava on the earth surface. It is one of the most common volcanic rock on earth with good mechanical, chemical, and thermal properties (Fiore et al. 2015). Basalt fibers are

manufactured by a process called continuous spinning where basalt rocks are melted in a furnace of 1450 - 1500 degrees Celsius and then forced through a platinum crucible to form fibers. The fibers can then be reshaped into chopped or continuous forms. The first recorded study on basalt fibers was conducted in the old Soviet Union in 1950 by the Moscow Research Institute of Glass and Plastic using it as a high-tech fiber for the defence sector. Its use as a construction material is relatively new with few researches conducted on its application for strengthening and rehabilitating reinforced concrete structures. A study conducted by Hughes (2018) showed that basalt fiber reinforced polymers (BFRP) fabrics have an ultimate stress of 460 MPa, elastic modulus of 21 GPa, and an ultimate strain of 2.35% making it very suitable for flexural strengthening of reinforced concrete beams. Some of the advantages of basalt fibers include: environmentally friendly, sustainable, corrosion-resistant, low cost of fibers due to low cost of production, abundant in nature, high chemical and thermal inertness, high ultimate strain at failure compared to other fibers, high strength-to-weight ratio, and low volume to weight ratio (making them easy to handle on site).

1.4 Finite Element Modelling

A thorough understanding of the behavior of the strengthening of a reinforced concrete beam is required to predict the behavior and the efficiency of the strengthening material. Although experimental studies provide a sound basis for understanding the behavior of reinforced concrete beams rehabilitated with basalt fibre fabric, numerical studies, however, provide the opportunity to predict and understand the effect of various parameters that would have been expensive to carry out experimentally. Finite element (FE) studies are used to numerically study the behavior of experiments carried out in the

lab where there is a variation of several parameters of which it would difficult and costly to conduct in the lab. Commercial FE software, Abaqus (Abaqus, 2018) was adopted for this study.

1.5 Objective

The objective of this study is to develop a finite element (FE) model capable of simulating the behavior of reinforced concrete beams externally strengthened with basalt fiber reinforced polymers (BFRP) and predicting the load-deflection responses, failure modes, ductility, cracking patterns and moment resistance of the strengthened beams.

1.6 Thesis Organisation

The thesis is written in the traditional format and is divided into six chapters. Chapter 1, the current chapter introduces the research intent and objectives. Chapter 2 presents a study of the available literature on the experimental procedure for strengthening reinforced concrete beams using various FRPs as well as the numerical studies conducted on them. Chapter 3 presents the experimental tests conducted to obtain the behavior of the beams as well as the tests conducted to obtain fracture parameters used for the finite element analysis (FEA). Chapter 4 focuses on the procedures taken for the FE modelling of the RC beam. Chapter 5 analyzes both the results obtained from the experiments as well as the results of the FE models. Chapter 6 presents the conclusions and recommendations for future studies.

CHAPTER 2
LITERATURE REVIEW

This literature review presents a summary of the studies that the author has found in literature on flexural strengthening of reinforced concrete beams using FRPs considering the various strengthening schemes and the failure mechanisms of the constituent materials.

2.1 Fracture Behavior

Structural analysis of materials using finite element method (FEM) require a good representation of the material properties. Accurate analysis and design of concrete structures is therefore, hinged on a proper understanding of the fracture behavior of concrete (Kotsovos and Newman, 1981). Fracture behavior of material deals with the initiation of fracture and propagation of cracks in a material. It plays an important role in predicting the mechanical performance of materials with discontinuity – an area where the classic strength of materials concept may not suffice as it assumes continuity in the material. It is able to predict the macroscopic mechanical behavior of materials by applying the theories of elasticity and plasticity to their microscopic defects (Kotsovos and Newman, 1981). Three modes of crack initiation are identified in fracture mechanics, namely: mode I, mode II and mode III. Mode I crack initiation occurs due to tension force normal to the crack plane, Mode II is caused by in-plane shear stresses and mode III is caused by out-of-plane shear forces. Figure 2.1a, Figure 2.1b and Figure 2.1c illustrate these three different modes of failure.

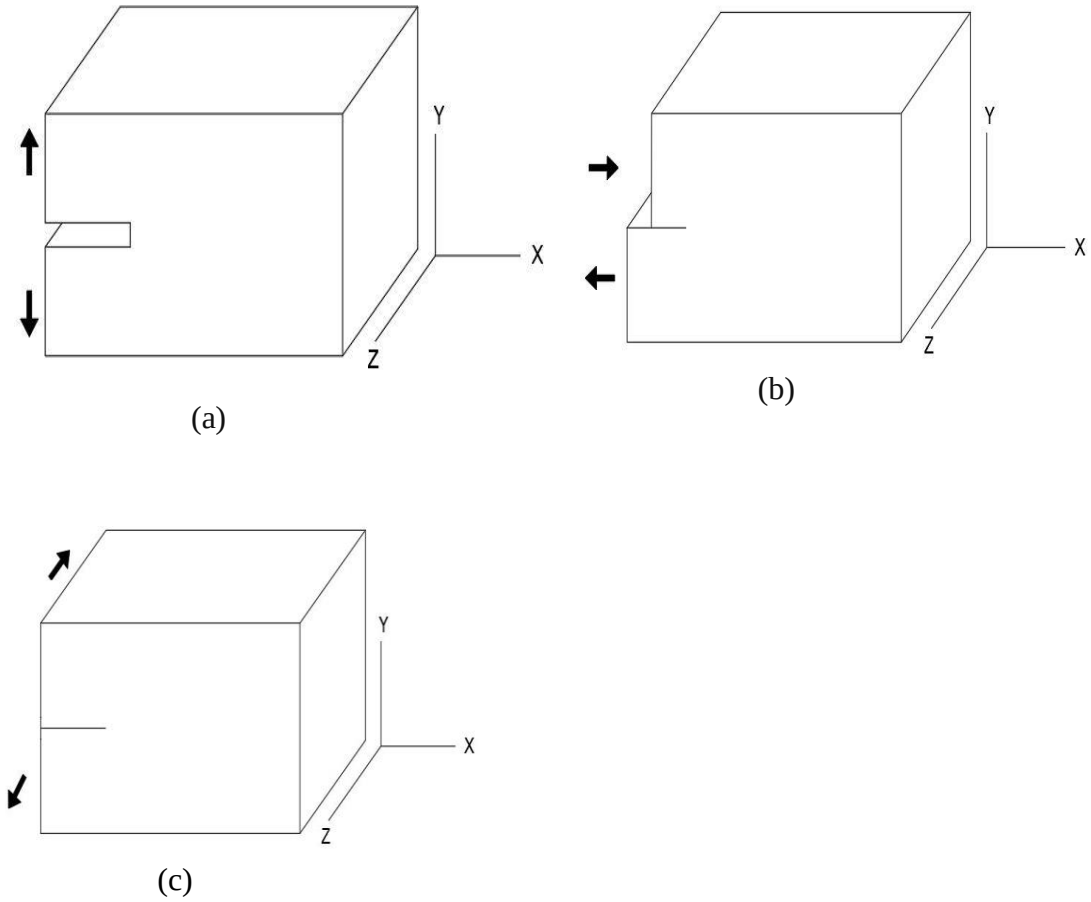

Figure 2.1: Failure modes (a) Mode I (b) Mode II (c) Mode III

This study is concerned only with mode I failure as the concrete beams are subjected to tension forces due to flexural loading. Fracture energy which is a vital non-linear fracture mechanics parameter was adopted to model the tensile behavior of the concrete specimens.

2.1.1 Fracture Energy

Fracture energy is the energy required to cause a unit surface area of concrete to crack. This fracture parameter plays a vital role in the representation of the softening behavior on the stress-strain curve of concrete under tension. It can be determined according to RILEM FMC-50 specification (RILEM, 1985) where a notched beam is subjected to

three-point loading as shown with Figures 3.10 and 3.11 in Chapter 3. The depth of the notch is between 0.45-0.55 of the beam depth (Uday, 2017). Fracture energy is calculated by dividing the area under the load–crack mouth opening displacement (CMOD) graph by the ligament area as shown in Equation 2.1.

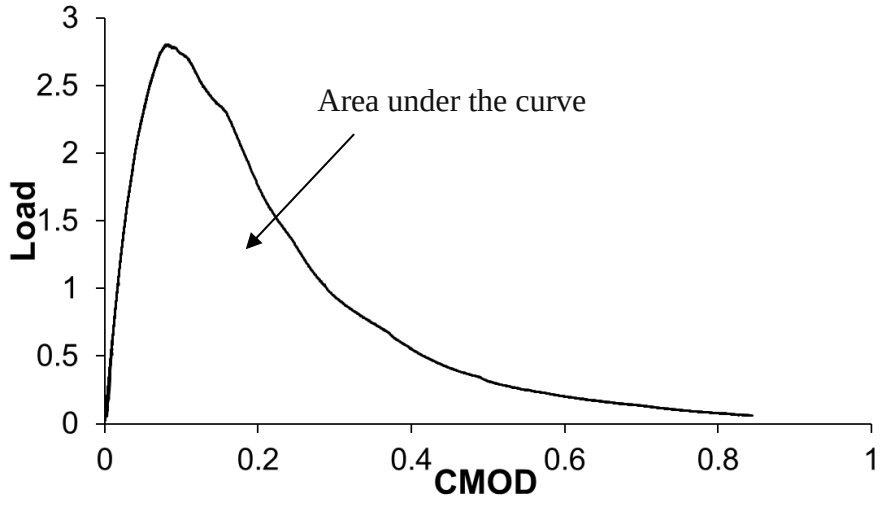

Figure 2.2: Load-CMOD graph

$$G_F = \frac{W_o}{A_{lig}} \tag{2.1}$$

where W_o is the area under the load-CMOD curve as shown in Figure 2.2 and A_{lig} is the area of the ligament of the specimen determined using Equation 2.2.

$$A_{lig} = (d - a)t \tag{2.2}$$

Where, d is the depth of the specimen, t is the thickness of the specimen and a is the notch depth.

2.1.2 Constitutive laws and material models

Constitutive laws are used to describe the relationship between two physical properties of a material showing its response to externally applied forces. They are essential in describing the behavior of materials experiencing deformations or strain under loading as the study conducted by Coronado and Lopez (2006) showed. The study investigated the effect of concrete constitutive behavior in numerical models of FRP strengthened reinforced concrete (RC) beams. Nonlinear material behavior, loading sequence, and crack propagation are some parameters that can affect the accuracy of the numerical model. The study observed that fracture energy is an important parameter required to predict crack propagation and debonding failure in the model. Although the model was not mesh dependent, the authors, Coronado and Lopez (2006) observed that using mesh size similar in magnitude to the coarse aggregate size produces good results in comparison with the experiments with a good prediction of the observed failure modes.

Linear and non-linear constitutive models can be applied to describe ductile and brittle materials. Constitutive laws form the frame work of the material models used in finite element analysis (FEA) and they consider both elastic and inelastic material responses. Linear elastic material models are used to describe the behavior of elastic materials that undergo small elastic strain ($\leq 5\%$) when loaded (Abaqus, 2018) These materials can be isotropic, orthotropic and anisotropic in nature, and are defined using Young's modulus (E), Poisson ratio (v), and shear modulus, (G) as constitutive relationships. Young's modulus, (E) which is based on Hooke's law is calculated using Equation 2.3. below.

$$\sigma = E\varepsilon \tag{2.3}$$

Where σ is the stress, E is the young's modulus and ε is the strain of the material.

Poisson ratio (υ) is the ratio between the lateral and longitudinal strain of a material subject to loading and shear modulus (G) is the ratio of the shear stress and strain in a material. The relationship between these constitutive coefficients is given in Equation 2.4.

$$G = \frac{E}{2(1+\upsilon)} \tag{2.4}$$

Materials with inelastic behavior are described in Abaqus using plasticity and damage models. Plasticity models are used for materials that do not experience loss of elastic stiffness before yield point during loading while damage models are used for materials with considerable reduction of stiffness in the elastic region due to loading (Abaqus, 2018). Plasticity models are formulated with an initial elastic response and assume that total deformation is made up of two parts as given in Equation 2.5.

$$F = F^{el} * F^{pl} \tag{2.5}$$

Where F is the total deformation, and F^{el} and F^{pl} are elastic and plastic deformations, respectively.

Plasticity models can be rate-dependent or rate-independent and are developed in terms of yield surface, flow rule, and hardening law. The yield surface determines the response of a material under purely elastic state of stress, the flow rule controls the inelastic deformation of the material after the yield point and the hardening law governs the transformation of the yield surface and flow rule after inelastic deformation (Abaqus, 2018). Steel reinforced bars are modelled using plasticity models while fiber reinforced

materials and quasi-brittle materials like rocks, mortar and ceramics are modelled with damage models.

2.2 FE Modelling

The choice of a strengthening scheme requires a good understanding of the behavior of the strengthening material before, during and after its application. This can be done through extensive experimentation which would be able to highlight the material properties and responses to different loading schemes and parameter changes. Although experimental testing provides a sound basis for understanding the mechanics of materials, it can be time consuming and expensive when an extensive parametric study is to be conducted. Finite element (FE) modelling and analysis can serve as an effective alternative to this rigorous experimental process, but it must be able to accurately represent the material and geometric properties of its constituent components and the interactions between them (Chowdhury, 1995; Chen et al., 2010)

2.3 Application of Finite Element Modelling

Finite element (FE) analysis has been used as an effective tool to study the behavior of various materials in a wide range of fields from civil, mechanical, oil and gas and biomedical engineering. Homogenous and non-homogenous materials such as steel, soils, bones, composites, and rocks with linear and non-linear material behavior have been represented using finite element models. Parashar and Sharma (2016) undertook a review of finite element models used to simulate the mechanical behavior of human bones and the joints when subjected to impact and fracture. Mechanical properties and the geometry of the bones were obtained using computed tomography (CT). The study concluded that with the recent improvements in biomechanics technology to determine bone properties,

finite element modelling will be effective in treating patients through the development of more effective fixation designs. Aresh et al. (2010) conducted a study on the behavior of rocks during the cutting stage using finite element modelling. Rock fracture mechanics was used to obtain the mechanical properties and failure mechanisms of the three different rock samples which was then applied to the model to simulate its behavior. FE modelling was an effective tool to understand some of the mechanics behind the rock cutting process. These studies among many others show that finite element modelling is a viable tool for predicting the behavior of complex materials provided the material properties can be adequately specified.

2.4 FE modelling of Concrete

Concrete is a heterogenous, quasi-brittle material with a non-linear behavior. One of the major limiting factors in the development of the finite element models for reinforced concrete is the complexity of concrete (ACI 446.3R-97; Chen et al., 2010). This complexity is due to the initiation and the formation of micro-cracks in concrete which is a major catalyst for potential structure failure (Uday, 2017). The proper representation of this non-linear complex behavior in the plastic region requires a good representation of cracking behavior of concrete using concrete cracking models.

2.5 Concrete Cracking Models

There are three crack models in Abaqus software capable of simulating concrete crack induced damage, namely: discrete crack model, smeared crack model, and concrete damaged plasticity model.

2.5.1 Discrete Crack model

This model treats cracks as geometric discontinuities or discrete gaps between elements with the same boundary. Cracks occur along the element boundaries when the nodal stresses normal to the element boundary is higher than the maximum tensile stress of the material (Abaqus, 2018). This model works well when the location of the crack is known in advance and is then followed by a series of re-meshing to simulate the crack propagation. The dependency of the results on the mesh size adopted and the high computational cost of re-meshing is a major drawback of this model (Chen et al., 2010).

2.5.2 Smeared Crack model

This model represents cracks as a continuum with an infinite number of parallel cracks distributed across it (Chen et al., 2010). It uses a constitutive relationship to represent the deterioration of the material stiffness. Shear retention factor and tension stiffening parameters are introduced into the model to account for the reduction of the shear stiffness and flexural stiffness of the concrete. The major concern of this model is the mesh dependency of its solution which is addressed using Hillerborg's (1976) fracture mechanics approach.

The two afore mentioned models are limited to crack simulation in plain concrete and cannot be applied to a study on reinforced concrete. Hence, a different model able to incorporate both the behavior of concrete and steel is required for the analysis.

2.5.3 Concrete Damaged Plasticity (CDP) model

This is a continuum model adopted for the simulation of reinforced concrete and other quasi-brittle materials in Abaqus. It was proposed and theoretically explained by Lubliner et al. (1989) and then developed by Lee and Fenves (1998). The irreversible degradation

of the modulus of concrete due to cracking is represented by the combination of isotropic damaged elasticity and multiple hardening plasticity (Abaqus, 2018). The model assumes that failure of concrete occurs when both tensile cracking and compressive crushing occurs. The development of these failures is due to the degradation of the elastic modulus of concrete which is characterised by the specification of damage parameters in tension and in compression. The damage parameters are functions of the plastic strain and can be calculated from the uniaxial tension and compression behavior as shown in Figures 2.3 and 2.4 using Equation 2.6 (Abaqus, 2018)

$$E = (1 - d)E_o \tag{2.6}$$

Where, E is the elastic modulus of the material after loading, E_o is the initial elastic modulus and d is the damage parameter (tension and compression)

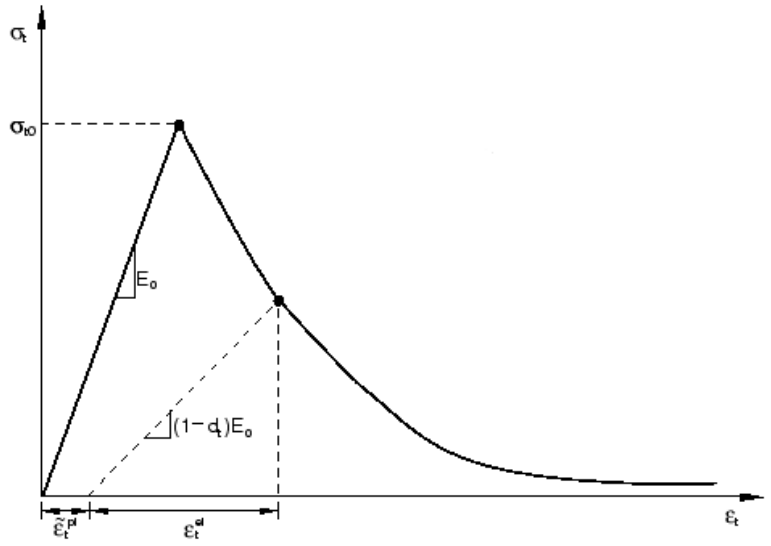

Figure 2.3: Response of concrete under uniaxial tension (Abaqus, 2018)

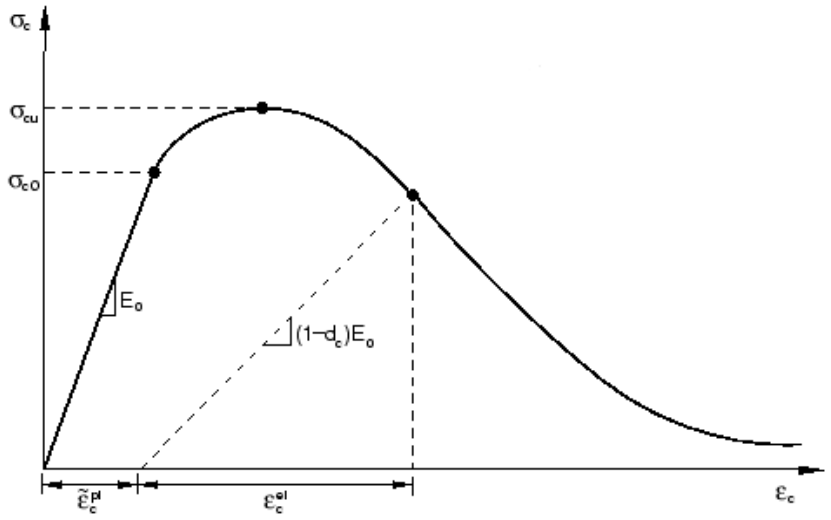

Figure 2.4: Response of concrete under uniaxial compression (Abaqus, 2018)

2.5.3 Tension Stiffening

Tension stiffening plays an important role in the analysis of reinforced concrete members as it simulates the interaction between the concrete substrate and the steel rebars when cracking occurs. It describes the strain-softening behavior of cracked concrete, ensures the transfer of loads and stress across the concrete through the rebars when cracks develop and helps model bond-slip effects and dowel action which may be associated with the concrete/rebar interface. Tension stiffening specification is important to ensure the overall stability of the analysis and is defined either by using a post-failure stress-strain table or fracture energy criterion (Abaqus, 2018). Fracture energy criterion adopts the (Hillerborg et al., 1976) fracture model which represents the cracking behavior of concrete with stress-crack opening displacement values obtained from fracture mechanics tests discussed later in Chapter 3.

2.6 FE modelling of Fiber Reinforced Polymers

This section discuses the finite element modelling and analysis of FRP showing the damage initiation and evolution criteria adopted.

2.6.1 Hashin's damage initiation criteria for FRP

Abaqus offers users one option for defining FRP behavior and damage using the Hashin's criteria (Abaqus, 2018). This criterion is adopted where more than one stress components is used to evaluate failure in a unidirectional fiber composite. It can be implemented with two- and three-dimensional problems involving laminates. The representation of damage initiation and evolution of fiber reinforced polymers is a critical factor in determining the accuracy of the model. Damage of fiber reinforced polymers in Abaqus refers to the gradual degradation of the material stiffness till the point of failure and it requires that the material exhibit a linear elastic behavior prior to damage (Abaqus, 2018). Since FRPs are the combination of fibers and matrix, failure needs to occur in both materials before the FRP fails. Failure initiation in FRP based on Hashin's criteria is divided into four different mechanism namely: fiber tension damage, fiber compression damage, matrix tension damage, and matrix compression damage. Equation 2.7 to Equation 2.10 present the failure initiation criteria for fiber in tension, fiber in compression, matrix in tension and matrix in compression, respectively.

Fiber in tension ($\sigma_{11} \geq 0$);

$$F_f^t = \left(\frac{\sigma_{11}}{X^T}\right)^2 + \alpha\left(\frac{\tau_{12}}{S^L}\right)^2 \tag{2.7}$$

Fiber in compression ($\sigma_{11} < 0$);

$$F_f^c = \left(\frac{\sigma_{11}}{X^C}\right)^2 \tag{2.8}$$

Matrix in tension ($\sigma_{22} \geq 0$);

$$F_m^t = \left(\frac{\sigma_{22}}{Y^T}\right)^2 + \left(\frac{\tau_{12}}{S^L}\right)^2 \tag{2.9}$$

Matrix in compression ($\sigma_{22} < 0$);

$$F_m^c = \left(\frac{\sigma_{22}}{2S^T}\right)^2 + \left[\left(\frac{Y^C}{2S^T}\right)^2 - 1\right] \left(\frac{\sigma_{22}}{Y^C}\right)^2 + \left(\frac{\tau_{12}}{S^L}\right)^2 \tag{2.10}$$

Where σ_{11} and σ_{22} are the normal stresses in x and y plane , τ_{11} and τ_{22} are the shear stress in the x and y plane, X^T is the longitudinal tensile strength, X^C is the longitudinal compressive strength, Y^T is the transverse tensile strength, Y^C is the transverse compressive strength, S^L is the longitudinal shear strength and S^T is the transverse shear strength.

2.6.2 Damage evolution criteria for FRP

Damage evolution of FRPs is specified using the fracture energy of the material. Fracture energy is the energy required to case complete failure of the BFRP laminate and it is calculated along the longitudinal tension, longitudinal compression, transverse tension and transverse compression axes using Equation 2.11.

$$G_f = \frac{l^* \sigma_u \varepsilon_u}{2} \tag{2.11}$$

Where, G_f is the fracture energy, l^* is the characteristic length which is a function of the mesh density, σ_u and ε_u are the ultimate stress and ultimate strain of the BFRP fabrics, respectively.

2.7 FE modelling of Reinforced Concrete beams

This section discusses previous finite element studies conducted on reinforced concrete beams highlighting the effects of some modelling parameters on the accuracy of the studies. Wahalathantri et al (2011) conducted a study on the elastic and plastic properties of concrete using two numerical models to develop the strain-stress curve of concrete. The numerical models developed by Nayal and Rasheed (2006) and Hsu and Hsu (2009) model provided stress-strain values of concrete in tension and compression. These values were applied to develop the FE model used to predict the behavior of reinforced concrete beams under flexural loading. The numerical models were able to simulate the effect of tension stiffening used to define the interaction between the steel reinforcement and concrete ensuring that load applied, and strain is transferred effectively through the steel rebars when cracking occurs. Although the model was limited to reinforced concrete without fibers, it showed a good correlation with the load deflection behavior and the crack initiation values of the experimental results.

Michał and Andrzej (2015) also studied the effects of some parameters of the concrete damaged plasticity (CDP) model in Abaqus on the accuracy of the analysis results. Among the parameters studied, the viscosity parameter, which make the constitutive models rate dependent and the dilation angle, which is the internal friction angle of concrete were found to play a major role in the initiation of cracks in the fracture process zone. Uniaxial and biaxial compression and test data were used to validate the numerical model. It was observed that a viscosity value greater than 0.0001 leads to a diffusion of the crack pattern and therefore, inhibits crack propagation while dilation angles of more than 5 degrees for confined structures leads to overestimation of the capacity.

Another study conducted by Earij et al. (2017) suggested a higher value for the dilation angle when there is no confinement of the concrete. Dilation angle of 40 degrees was adopted for this study based on a sensitivity analysis conducted, which showed a significant loss of ductility (about 40%) when lower values of dilation angle are used for unconfined concrete structures. Other modelling parameters were adopted as recommended by (Abaqus, 2018).

2.8 FE modelling of Reinforced Concrete strengthened with FRP

There have been several finite element studies conducted on strengthening reinforced concrete structures for shear and flexure using various fiber fabric. This section discusses some of these methods such as two-dimensional and three-dimensional models as well studies carried out using carbon, green-natural, and glass fiber-based fabrics as strengthening materials.

2.8.1 Finite Element analysis using two-dimensional models

Chen et al., (2010) developed a two-dimensional smeared crack model to represent non-linear behavior of reinforced concrete beams strengthened for shear with FRP fabric. Abaqus Explicit was adopted to solve the convergence problem encountered in modelling cracks and debonding. The study observed that a proper representation of the interaction between the three elements: concrete, steel, and FRP is important to obtain an accurate representation of the shear behavior of the beams. An inappropriate interaction would lead to an overestimation of the beam capacity and crack formation. When compared with the experimental data, the FE model with five layers of FRP strengthening had the closest correlation, as the results were 6.7% higher than the test results. The model was also able to predict the failure modes and cracking pattern.

2.8.2 Finite Element analysis using three-dimensional models

Earij et al. (2017) studied three-dimensional nonlinear modelling of two reinforced concrete beams under a loading–unloading–reloading condition. The study adopted the concrete damaged plasticity (CDP) model using Abaqus Explicit to simulate the behavior of the reinforced concrete beams. Post-failure stress-strain relationship was used to define the load-deflection response of the beams in the plastic regions. The effect of using truss or beam elements to model steel reinforcement, effect of the shape of the tension softening laws, and the effect of different element types on the results were examined. The study compared the effect of using three tension stiffening laws, linear, bi-linear and exponential response and observed that they were all in good agreement with the test, however, the linear tension stiffening law had a slightly stiffer response before yielding occurred. Both structured and unstructured mesh types showed a good correlation with the load-deflection values obtained from the experiment but for crack patterns, structured mesh exhibited a mesh bias. Using beam elements for modeling steel rebar were concluded to be better for models with geometrical non-linearity as truss elements experience large strains and subsequent reduction in cross section thus reducing the load capacity.

Hawileh et al. (2013) investigated the FRP fabric debonding failure mode of reinforced concrete beams strengthened for shear with short length CFRP fabric using finite element modelling. The study was conducted on CFRP fabric with two different lengths (25% and 85%) of the shear span of the beams. Non-linear constitutive laws were incorporated into the model to simulate the interaction between the parts of the model with consideration made for bond-slip. The study concluded that increasing the tension steel diameter

reduces the beam ductility which leads to sudden plate debonding failure. This can be delayed using transverse cross straps of 400 mm width on the beam which were represented accurately in the model.

Obaidat et al. (2010) examined the behavior of reinforced concrete beams with cross sectional area of 300 x 150 mm and length of 1960 mm retrofitted with 1.2 mm thick CFRP plates using finite element analysis. Concrete damaged plasticity model was adopted for the analysis with the interface between the concrete and CFRP plates modelled with both a perfect bond and cohesive bond. Fracture energy was used to represent the behavior of the concrete in tension as opposed to the post-failure stress-strain curve which is difficult to obtain. The modelling of the concrete-CFRP interface with a cohesive bond was observed to be better than the perfect bond at predicting the debonding failure of the CFRP from the concrete. Three different lengths of the CFRP plates were tested, 520 mm, 1040 mm and 1560 mm and it was observed that the ultimate capacity of the beams increased with the length of the CFRP plates. There was a good correlation between the FE model and the experiment in terms of the ultimate capacity, cracking patterns, and failure modes.

Głodkowska and Ruchwa (2010) developed a model to simulate the changes in displacement and the evolution of material damage in CFRP strengthened beams for flexure using Abaqus/Explicit (Abaqus, 2018). The model accurately predicted the initiation of the cracks like the experiments but showed disparities as the crack propagated to the ultimate failure. This disparity was presumed to occur due to an underestimation of the damage parameters of the concrete showing that a good approximation of damage parameters is important for accuracy in the results. The study

observed that strengthened beams were able to sustain more cracks, possess higher load capacity, and withstand more deflection than unstrengthened beams with a further increase in the capacity through the use of transverse CFRP fabrics.

Pham and Al-Mahaidi (2005) developed a non-linear FE model to study the behavior of reinforced concrete beams retrofitted with CFRP fabrics for flexure. Smeared crack model was adopted for the study using FEA software DIANA (DIANA, 2017) with interfacial elements to model the bond between concrete and reinforcement. The failure mode observed for beams retrofitted with one to three layers of CFRP fabric was debonding in the span, while beams with more than three layers of CFRP experienced debonding failure at the ends of the beam. The results of this paper indicate that the optimum number of layers CFRP fabric, which can be used to strengthen a beam without the use of cross straps is three. The length of the CFRP fabric was inversely proportional with the debonding capacity of the beams.

Cervantes et al. (2014) conducted an experimental and numerical study on the use of green natural fiber reinforced polymer (GNFRP) to strengthen concrete beam in flexure. GNFRP are bio-composites made from biodegradable components adopted to reduce the negative environmental impacts, which are caused during the production and disposal of synthetic fibers. The design was checked with ACI 440.2 R-02 (2002) code for the flexural strengthening of concrete using FRP.

$$M_n = A_s f_s \left(d - \frac{\beta_1 c}{2} \right) + \Psi_f A_f f_{fe} \left(h - \frac{\beta_1 c}{2} \right)$$

The study was done with 10 layers of GNFRP and observed a 68% increase in the beam flexural capacity while ductility decreased by 25% (50.8 mm to 40.4 mm) compared to

the unreinforced control specimen. The ultimate strain of GNFRP fibers at rupture was 1.4%, which is higher than carbon whose ultimate strain is 0.9%, presenting it as a viable option for the strengthening of concrete beams.

Radfar et al. (2012) studied the numerical modelling of concrete cover separation failure of reinforced concrete beams strengthened with FRP. Concrete cover separation failure is a premature failure mode whereby the concrete cover peels off from the steel reinforcement at the ends of the beam. This failure mode occurs suddenly and prevents the concrete from attaining its maximum strength. Three-dimensional nonlinear FE models were developed and used to simulate a quarter of the beam size to predict its flexural behavior under a four-point bending scheme. The study adopted fracture energy approach incorporating tension stiffening into the model to simulate the transfer of stresses in concrete along the steel reinforcement after crack formation. The study observed that the maximum error between the FE model and the test in the prediction of ultimate load was 14%, with the FE model being higher. For the deflection values, the maximum error was 17.9% with the FE model being the lower of the two. This was presumed to be due to an over approximation of the concrete strength after the crack formation.

Sagher and Abed (2017) carried out a study on shear strengthening of short reinforced concrete beams using glass fiber reinforced polymer (GFRP) rods. The GFRP rebars were used in place of steel rebars as tension reinforcement. The FE model included geometry and material nonlinearity using a 20 mm sized mesh. The study found that the shear strength of the strengthened beams increased by 33% when the reinforcement ratio

of the GFRP rebars increased from 0.26% to 1.64% resulting also in the reduction of the mid-span deflection of the beam by more than 50%.

2.9 FE Basalt Fiber Reinforced Polymers

The application of basalt fabric for strengthening reinforced concrete structures is still in its development stages when compared to glass and carbon fibre fabrics. Experimental studies were conducted to understand the structure, properties and advantages in order to determine its effectiveness as a strengthening material.

Fiore et al. (2015) observed that basalt fibre would be relatively cheaper than glass and carbon fiber fabrics since it requires low energy and no additives during the manufacturing process. The lower cost of production along with its higher thermal insulation and higher ultimate strain make basalt fibre fabric a good choice for flexural and shear strengthening of reinforced concrete. Sim et al. (2005) conducted an experimental study on the durability of basalt fabric and its application in strengthening reinforced concrete beams. The durability of basalt fibers fabric was examined by weather resistance test, alkali resistance test, and thermal stability test and the test data were compared to similar test data obtained from carbon and glass fabric. The studies observed that though carbon fibers possessed higher alkali and weathering resistance than basalt and glass fibers, the thermal stability test showed basalt fabric to be the better of the three samples with a 10% reduction of strength when exposed to temperature over 600 degrees while carbon and glass fibres melted in the heat. In addition, for strengthening reinforced concrete beams, basalt fibers were more effective in reducing catastrophic debonding failure due to higher ultimate strains, with two layers providing the best efficiency.

Lihua et al. (2013) investigated experimentally on the use of BFRP fabric for flexural strengthening of reinforced concrete beams. The results were compared with similar concrete beams strengthened with CFRP and GFRP fabrics. The study found that beams strengthened with BFRP fabrics had a larger ultimate strength in comparison to beams strengthened with GFRP, but lower strength in comparison to beams strengthened with a similar layer of CFRP fabric. In comparison with the control specimen, the ultimate strength of reinforced concrete beams strengthened with CRFP, BFRP, and GFRP was 25%, 18% and 20% respectively.

This study also observed that the use of cross straps as endpoint anchorage was more effective in increasing the load capacity of the beam than having it across the whole length of the beam. This was because the latter induces high strains in the laminates near the concrete cracks, which resulted in a sudden brittle failure. One of the limitations of the study was the maximum number of plies tested, which was two. The study concluded that two plies of BFRP fabric were more effective in improving the load capacity and limiting crack formation than one ply. In addition, analytical models developed to predict debonding strain values for CFRP were compared to the debonding strain values of BFRP obtained from the experiment. The results showed that the analytical models could predict only 60% of the debonding strain values of the BFRP fabric because the models do not account for the higher ultimate strain values of the basalt fabric. The results indicate that although the analytical models can be extended to BFRP strengthening schemes, it is very conservative.

In a study conducted by Abed and Alhafiz (2018), a finite element model was developed to simulate the flexural behavior of reinforced concrete beams using basalt rebars in place

of steel as longitudinal reinforcement. The non-linear model predicted an increase in the flexural strength of the beam with increasing reinforcement ratio as observed in the experimental results. Also, the addition of chopped basalt fibers into the concrete mix was observed to improve the ductility of the beams by 30% when compared to the control.

2.10 Summary

Literature review found that finite element studies have been conducted using CFRP, GFRP and GNFRP fabric and rebars to strengthen reinforced concrete beams for flexure and shear. The results obtained show that they are a viable option for strengthening reinforced concrete beams providing a significant improvement in ultimate capacity, however, with a reduction in beam ductility due to lower ultimate strain values of the FRP. Basalt fibers are low-cost, fire-resistant, naturally abundant fibers possessing high strength to weight ratio and higher ultimate strain compared to carbon and glass fibres making it a good option for flexural strengthening of concrete. Literature review found a limited number of experimental studies using BFRP rebars and basalt chopped fibers to strengthen reinforced concrete beams, which showed similar increases in the ultimate strength of the beams but also an improvement in the ultimate ductility. To the best of the authors knowledge, no FE studies have been conducted using BFRP fabrics as a strengthening material.

CHAPTER 3
EXPERIMENTAL METHODOLOGY

3.1 General

The objective of this thesis is to develop finite element (FE) models to simulate the behavior of reinforced concrete beams externally strengthened with basalt fiber reinforced polymers (BFRP) fabric. The commercial finite element analysis software, Abaqus (Abaqus, 2018) was adopted to predict the responses and efficiency of the flexural strengthening scheme. In order to have a FE model with a good representation of the behavior of concrete, mechanical properties of concrete, steel, and BFRP were obtained. The methodology was broken down into two parts, which are experimental and finite element modelling (which will be discussed in Chapter 4).

Two phases of experimental testing were performed. Phase 1 of the experimental methodology involved material testing to obtain the parameters required for the development of the finite element model. Phase 2 of the experimental methodology was structural testing on beam specimen to validate the finite element model. Beam tests of Phase 2 were completed by Hughes (2018); however, only selected test data are used in the current study for validation of the FE models.

3.2 Material Testing

Material testing was performed on concrete, steel, and BFRP fabric. The material properties of concrete were determined. Six different tests were performed on the concrete which include compressive test, cyclic compressive test, split tensile test, direct tensile test (DTT), wedge split test (WST), three-point bending (TPB) on notched specimens. Uniaxial tension testing was performed on steel and basalt fiber fabric. Figure

3.1 and Table 3.1 presents the specimens and summary of the tests carried out and the parameters evaluated.

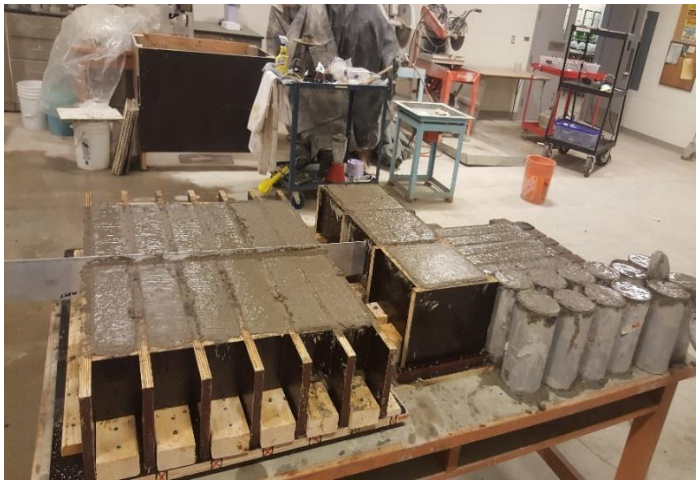

Figure 3.1: Casting of Specimen for Phase one

Table 3.1: Summary of material tests

Material	**Test**	**Standard**	**FE Parameter**
Concrete	Uniaxial monotonic compression	ASTM C39	Ultimate compressive stress (σ_{cu})
	Uniaxial cyclic compression	ASTM C39	Compressive damage parameter (d_c)
	Direct tensile	FHWA HRT - 17-053	Ultimate tensile stress (σ_{tO})
	Split tensile	ASTM C496	Ultimate tensile stress (σ_{tO})
	Wedge splitting	RILEM TC 89-FMT	Tensile damage parameter (d_t)
	Notched 3-point bending	RILEM FMC 50	Fracture energy (G_f)
Steel	Direct tensile (coupon test)	ASTM A370-18	Elastic and plastic stress- strain behavior
Basalt fabric	Direct tensile (coupon test)	ASTM D3039	Stress and strain responses

3.2.1 Concrete Compression Tests

Uniaxial monotonic and cyclic compression tests were performed to determine the compressive behavior of concrete in the elastic and plastic regions. For both tests, the 28-day compressive behavior of three capped cylinders with a diameter of 100 mm and length of 200 mm was determined in accordance with ASTM C39/C39M (ASTM, 2018b). A universal testing machine was used to apply load at a rate of 0.25 MPa/s on the concrete cylinder until failure occurs while the load and actuator displacement was recorded. The average ultimate compressive strength of the concrete mix (σ_{cu} as shown in Figure 2.5) was obtained from the stress and strain curve as shown in Figure 3.2.

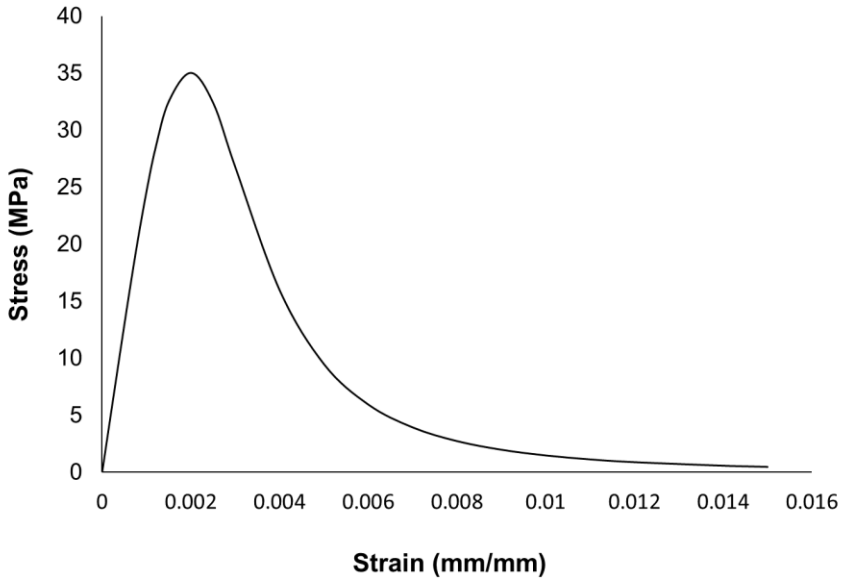

Figure 3.2: Compressive stress-strain behavior of concrete

A compressive cyclic loading test was undertaken to determine the degradation rate of the elastic modulus of concrete in the plastic region. The specimens were subjected to cyclic loading after reaching ultimate stress. As the concrete specimen undergoes loading and unloading, the value of the modulus reduces, and the rate of

reduction can be used to determine the compressive damage parameter of the concrete. The compressive damage parameter, d_c as shown in Figure 2.5 was obtained from the stress-strain curve of the specimens (Figure 3.3) and Equation 3.1.

$$d_c = 1 - \frac{E}{E_0} \tag{3.1}$$

The term d_c is the compressive damage parameter, which indicates the scalar degradation of the concrete. The term E_0 is the initial (undamaged) modulus (see Figure 3.3), which is obtained from the slope of the stress-strain curve in the elastic region. Lastly, the term E represents the reduced modulus obtained from the slope of each load-unload cycle.

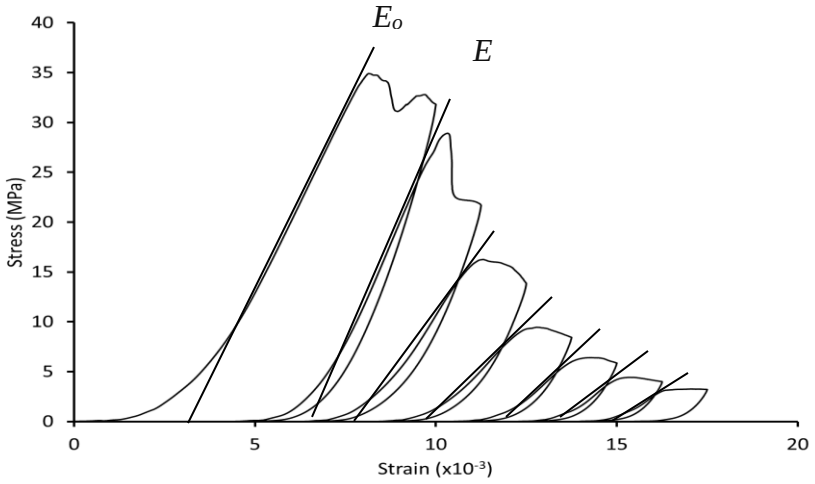

Figure 3.3: Typical monotonic cyclic loading curve

3.2.2 Concrete Tension Tests

The tensile strength of the concrete sample was determined using both direct and indirect (split tensile test) tensile tests. Concrete is a non-homogenous material with weak tensile properties and brittle behavior. This behavior makes it difficult to calculate its tensile strength resulting in the absence of a generally accepted standard on a direct way to calculate it. The direct test developed by Graybeal and Baby (2014) and adopted by the

Federal Highway Authority (FHWA, 2019) was used in this study as the direct method for determining the uniaxial tensile strength (f_t). Although the test was designed for calculating the tensile strength of ultra high-performance concrete (UHPC), it was adopted to verify its effectiveness for medium strength concrete. The indirect method adopted was the split tensile test developed by Carneiro and Barcellos (1949). This test was done according to ASTM C496/C496M-17 (ASTM, 2017a). Due to the possibility of specimen misalignment, stress concentration at the grips, and self-weight problems, the split tensile test was conducted to verify the direct tensile test results (Nilson and Winter, 1991; Østergaard et al.2003).

3.2.2.1 Direct Tensile Test

Four concrete specimens with length of 440 mm and cross-sectional area of 50 mm x 50 mm were cast. Prior to testing, the sides of the specimens were given a light sanding before being attached to aluminium grips which had been cleaned with acetone to remove any impurities. The aluminium grips with dimension of 170 x 50 mm and 3 mm thickness were then attached to the sides of the concrete specimen using an epoxy resin and cured for at least 12 hours. The specimens were then mounted into aluminium grips which were aligned with a spirit level. The proper alignment of the specimen is of vital importance as misalignment can lead to eccentric loading which can result in the premature failure of the specimen and incorrect tensile strength values (Graybeal & Baby, 2014). The test specimen and the test setup are shown in the Figure 3.4. The gage length of the specimen was maintained at 100 mm giving enough distance for the concrete to fail within it. The specimens were subjected to uniaxial tension using the

universal testing machine with a displacement-controlled load and a loading rate of 0.001 mm/s. The maximum tensile stress was obtained from the stress and strain graph.

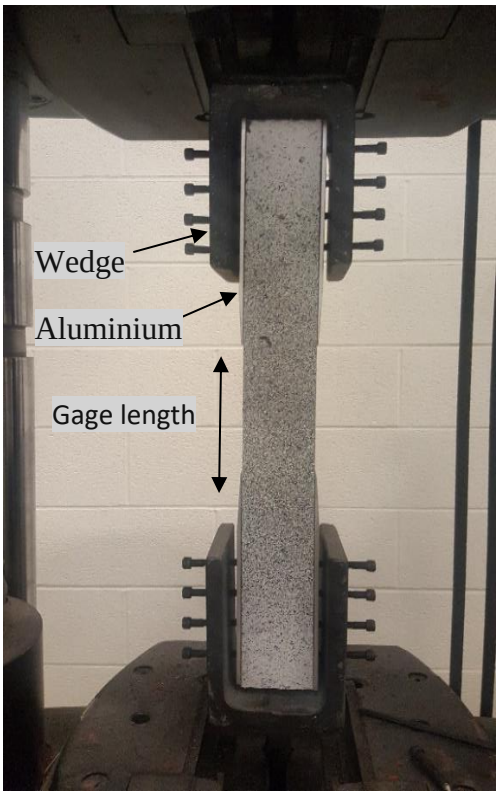

Figure 3.4: Direct Tension Test

3.2.2.2 Split Tensile Test

This is an indirect method for calculating the maximum tensile strength of concrete. The results obtained from this test play an important role in determining the initiation of a crack in concrete beams. Crack initiation occurs when the tensile forces at a point in the concrete exceed the specified tensile strength at the same point and in the same direction.

The split tensile test was set up as specified by ASTM C496/C496M-17 (ASTM, 2017a) with a cylindrical specimen of 200 mm height and 100 mm diameter. After 28 days of curing, the specimen was mounted between two platens with a strip of wood placed between the concrete and the platen, as shown in Figures 3.5 and 3.6. The strip of wood was placed between the specimen and the steel platens to reduce the high stress concentrations along the axis of loading, and to ensure a uniform distribution of the load along the specimen. The split tensile strength (as shown in Figures 3.5 and 3.6) of each specimen obtained after the split of the specimen as shown in Figure 3.7 was determined using the equation developed by Timoshenko and Goodier (1970). This split tensile strength is presented in Equation 3.2 below:

$$f_{sp} = \frac{2P}{\pi l d} \tag{3.2}$$

Where f_{sp} is the split tensile strength in MPa, P is the maximum load applied by the testing machine in kN, l and d are the length and diameter of the specimen respectively in mm.

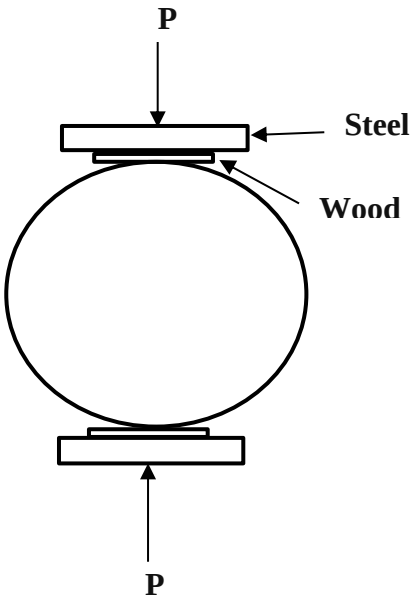

Figure 3.5: Scheme of Split Tensile test

The value of the split tensile strength (f_{sp}) is usually higher than the uniaxial tensile strength (f_t) obtained from direct test because the stress distribution induced by the diametric loading of the specimen is not always uniform on the specimen. A total load reduction factor of 17 percent was applied on the load value obtained in the testing, of which 12 percent (as specified by Neville 1981) was to account for the material dependency of the test while the 5 percent was due to the size effect of using a smaller sample as stated by Blanks and Mcnamara (1935). This was applied to the experimental results of the split tensile strength to convert it to the true tensile strength. Three samples were tested to obtain the split tensile strength.

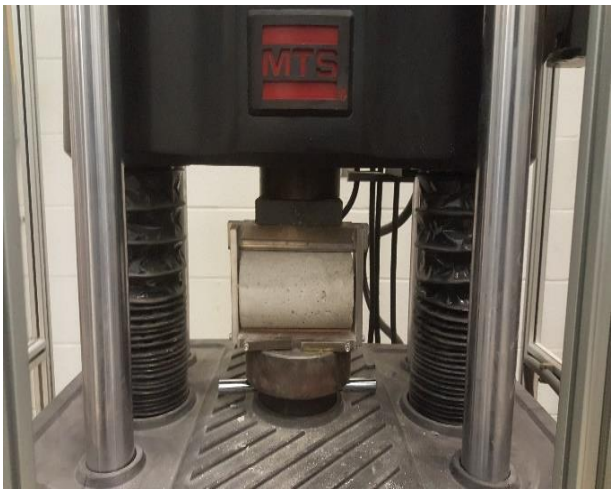

Figure 3.6: Split tensile test

Figure 3.7: Specimen after test

3.2.3 Concrete Fracture Tests

Fracture properties of concrete can be determined through the wedge splitting test (WST) and three-point bending test (TPBT) on notched specimens. WST is an indirect method used to determine concrete tension damage properties required for the FE model. This is done by the obtaining the vertical load (P_v) and crack mouth opening displacement (CMOD) values from the experiment. The vertical load (P_v) is converted to the splitting force P_{sp} which is the horizontal force component required to cause the wedge to split calculated with Equation 3.3. The P_{sp}-CMOD plot is converted into stress(σ)- deformation (w) curve through inverse analysis.

$$P_{sp} = \frac{P_v}{2tan\alpha} \tag{3.3}$$

Where α is the angle of the loading plate given as 15 degrees

3.2.3.1 Wedge Splitting Test (WST)

The setup was done in accordance with RILEM TC 89-FMT (1991). The specimens tested had dimensions of 200 x 200 x 200 mm with a notch length and ligament length of 40 mm and 130 mm, respectively as shown in Figures 3.8 and Figure 3.9. One of the important factors that affect the WST is the angle of the loading wedge. The wedge angle plays a significant role in the behavior of the specimen as it affects both the stability and the frictional force between the specimen and the testing machine. A wedge angle of 15 degrees was adopted for the loading device based on RILEM TC 89-FMT (1991). For testing, the specimen was placed on a plate with pin support at the middle to allow for rotation about its axis, this ensured that the loading was symmetric on the bearing rollers and there was no unwanted restraint of the specimen. Vertical load and crack mouth opening displacement (CMOD) were then obtained from the testing machine and the clip gauge to obtain the P_{sp}-CMOD plot.

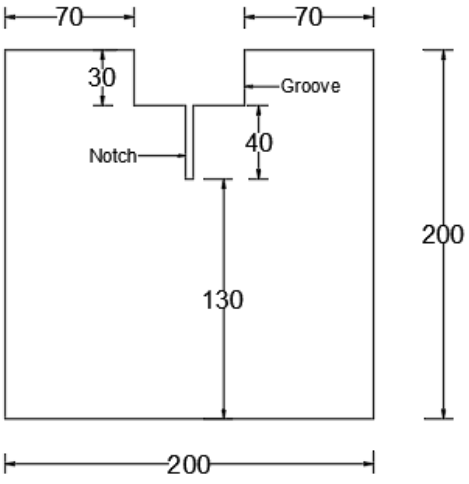

Figure 3.8: WST specimen dimensions

Figure 3.9: Wedge split test setup

3.2.3.2 Three Point Bending with notch Test (TPBT)

The TPBT was performed in accordance with RILEM-FMC 50 (1985) Three beam specimens with dimensions of 650 x 150 x 80 mm, clear span of 600 mm and notch depth of 75 mm, as shown in Figures 3.10 and 3.11, were subjected to three point bending under a load actuator with a displacement-controlled loading at a rate of 0.005 mm/s. The top of the specimens was cleaned to remove any dust and knife edges were attached to them by the edges of the notch with an epoxy. To measure the CMOD, a clip gauge was placed on the knife edges and was connected to the testing machine to record the CMOD. The values of the P-CMOD were obtained from the experiment and used to calculate the fracture energy (G_f) using Equation 3.4.

$$Gf = \frac{W1}{(d-a)T} \tag{3.4}$$

Where W is the work of fracture (area under the Load -CMOD curve), a is the notch depth in mm, d is the depth of specimen in mm and T is the thickness of the specimen in mm.

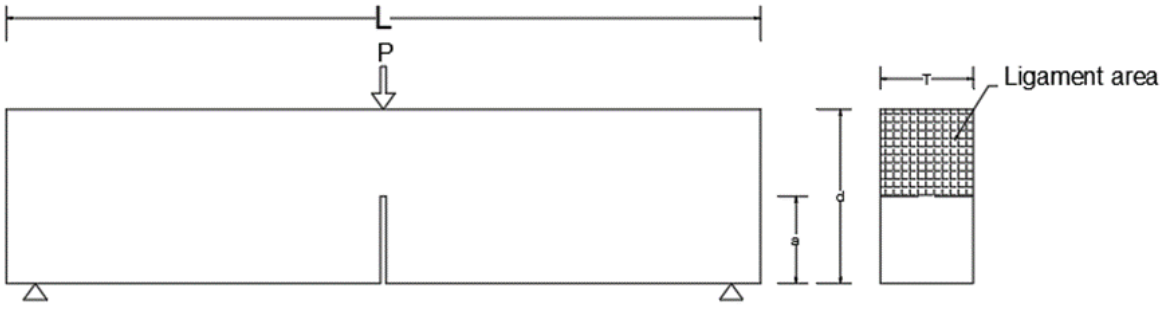

Figure 3.10: Scheme of the TPBT

Figure 3.11: TPBT set-up

3.2.4 Steel Reinforcement Test

The material properties of the steel reinforcements (10M and 15M rebars which have cross-sectional areas of 100 mm^2 and 200 mm^2, respectively) were determined by the uniaxial tension test. These properties which were obtained from the stress-strain response of the reinforcement include the elastic modulus, yield stress, ultimate stress, and post-yield stress-strain response.

The test setup as shown in Figure 3.12 followed ASTM A370-18 (ASTM, 2018a) recommendations. Specimens were cut to a length of 200 mm having a gauge length of 50 mm (which is about 4 times the nominal diameter of the bar as recommended by the standard) at the center. The gauge length at the center had a reduced cross-sectional area of not more than 1% of the cross-sectional area of the ends of the specimen as shown in Figure 3.13. This reduced cross-section was adopted to ensure the fracture occurs within it allowing for the ease in calculating the strain. A 50 mm extensometer was attached across the gauge length to measure the change in length. Uniaxial tension test was carried

out on a total of six specimen using a hydraulic machine with capacity of 250 kN and loading rate of 2.5 mm/min.

Figure 3.12: Steel rebar test

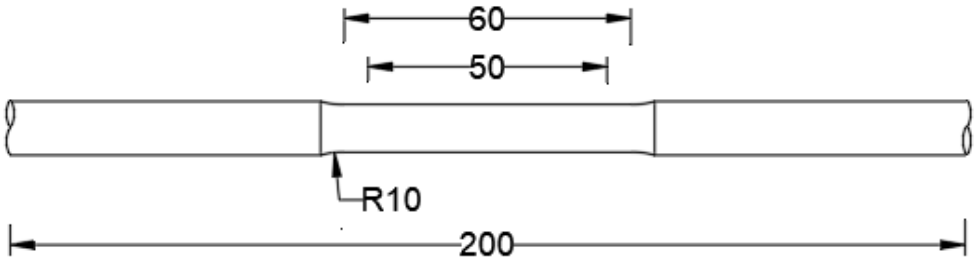

Figure 3.13: Steel rebar specimen dimensions

3.2.5 Basalt Fibre Coupon Test

The in-plane tensile properties of the BFRP fabric were determined using coupon tests in accordance with ASTM D3039/D3039M-17 (ASTM, 2017b). BFRP fabric were cut into rectangular coupons specimen each with a length of 200 mm and cross-sectional

area of 30 x 0.45 mm. Coupons specimen with 2, 4, 6, and 8 layers of BFRP fabrics were then subjected to a uniaxial tension loading. Plastic tabs were attached at the ends of the fibres using an epoxy resin to prevent griping damage during testing. The basalt coupons, as shown in Figure 3.14, were mounted in the grips of a 250 kN capacity hydraulic testing machine with a displacement rate of 2 mm/min. Figure 3.15 presents the typical fracture of the coupons after testing.

Figure 3.14: Basalt coupon under uniaxial tension test

Figure 3.15: Basalt coupons after uniaxial testing

3.3 Structural Testing

3.3.1 Four-Point Bending Test

The purpose of the structural testing was to validate the finite element models in predicting the behavior and damage of the strengthened beams. This validation was performed using experimental results obtained from four-point bending tests of 12 full-scale reinforced concrete beams. These beams were tested by (Hughes, 2018). Prior to using these test results, two smaller unstrengthened reinforced concrete beams with length of 1600 mm, and cross-sectional area of 150 x 150 mm were tested in the current study and the test data were used for the initial validation of the FE model. Upon the successful validation of the model using the load-deflection results of these two unstrengthened beams, the model was developed for the 12 full-scale beams which were tested by Hughes (2018). Table 3.2 summarizes the 12 beams each with length of 2400 mm, clear span of 2190 mm and cross-sectional area of 250 x 200 mm as shown in Figure 3.16. The beams were designed according to Canadian Concrete Structures Design

Standard CSA A23.3-14 (CSA, 2014) with a higher shear capacity than the flexural capacity to ensure flexural failure. The number of BFRP layers to be applied to increase the flexural strength of the beams by 50% was estimated using guidelines of CSA S806-12 (CSA, 2012). The layers of the BFRP were then varied to study their effects on the strength and deflection of the beams.

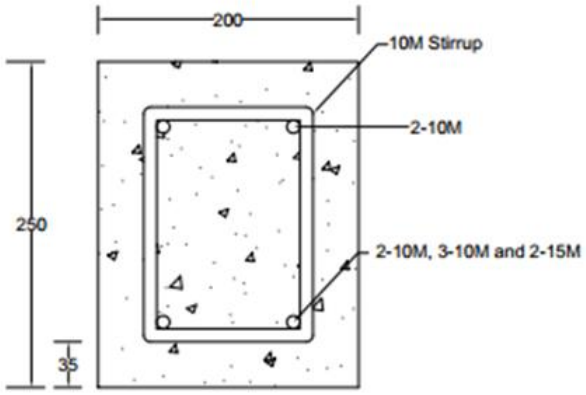

Figure 3.16: Beam cross section (adapted from Hughes, 2018)

Table 3.2: Experimental Test Matrix (Hughes, 2018)

Beam ID	Reinforcement ratio (%)	Number of layers
0.5RR- Control	0.5% (2-10M)	0
0.5RR-B02	0.5% (2-10M)	2
0.5RR-B04	0.5% (2-10M)	4
0.5RR-B08	0.5% (2-10M)	8
0.75RR- Control	0.75% (3-10M)	0
0.75RR-B02	0.75% (3-10M)	2
0.75RR-B04	0.75% (3-10M)	4

0.75RR-B08	0.75% (3-10M)	8
1RR- Control	1.0% (2-15M)	0
1RR-B04	1.0% (2-15M)	4
1RR-B06	1.0% (2-15M)	6
1RR-B08	1.0% (2-15M)	8

The beams were designed with a concrete mix having a compressive strength of 30 MPa and with a length to depth ratio of 9.6 to ensure that it remains flexurally dependent. The test matrix comprised of a total 12 beams divided into three groups of four beams each with a different reinforcement ratio (0.5%, 0.75% and 1%) and varying number of layers of the basalt polymers. The reinforcement ratios are calculated using Equation 3.4.

$$\rho = \frac{A_s}{bd} \tag{3.4}$$

Where ρ is the reinforcement ratio, A_s is the cross-sectional area, b and d are the beam width and depth respectively.

Shear reinforcements were provided as determined by CSA A23.3-14 (CSA, 2014) to ensure that the shear capacity of the beams was much higher than the flexural capacity. Figure 3.17 shows a profile of the reinforcements with all the dimensions in mm. After casting, the beams were then cured for 28 days before the BFRP fabrics were applied to the bottom side (tension face) of the beams using an epoxy resin. The BFRP fabrics were applied longitudinally across the tension face and orthogonally as cross-straps at the ends of the clear span just before the supports to ensure that delamination of the fabrics did not

occur. All beams were tested under four-point bending load using a displacement–controlled method with a loading rate of 2 mm/min. Figure 3.18 shows the four-point bending test setup used. Test data of the strain, load, and displacements were obtained from the strain gauges, load cell, and linear variable displacement transducer (LVDT) which were recorded using a computerised data acquisition system (DAQ). The load-deflection response of the beams, the failure modes, and the beam crack patterns obtained through digital image correlation (DIC) were then compared with the results obtained from the model for validation.

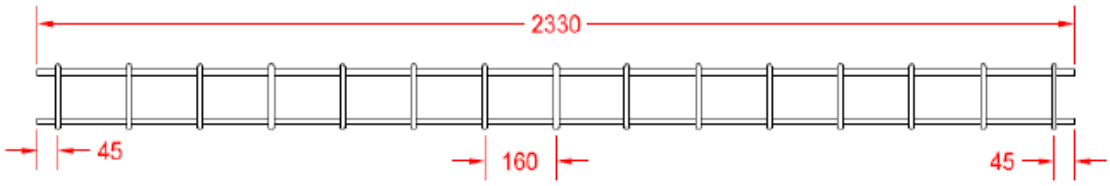

Figure 3.17: Steel rebar profile (Hughes, 2018)

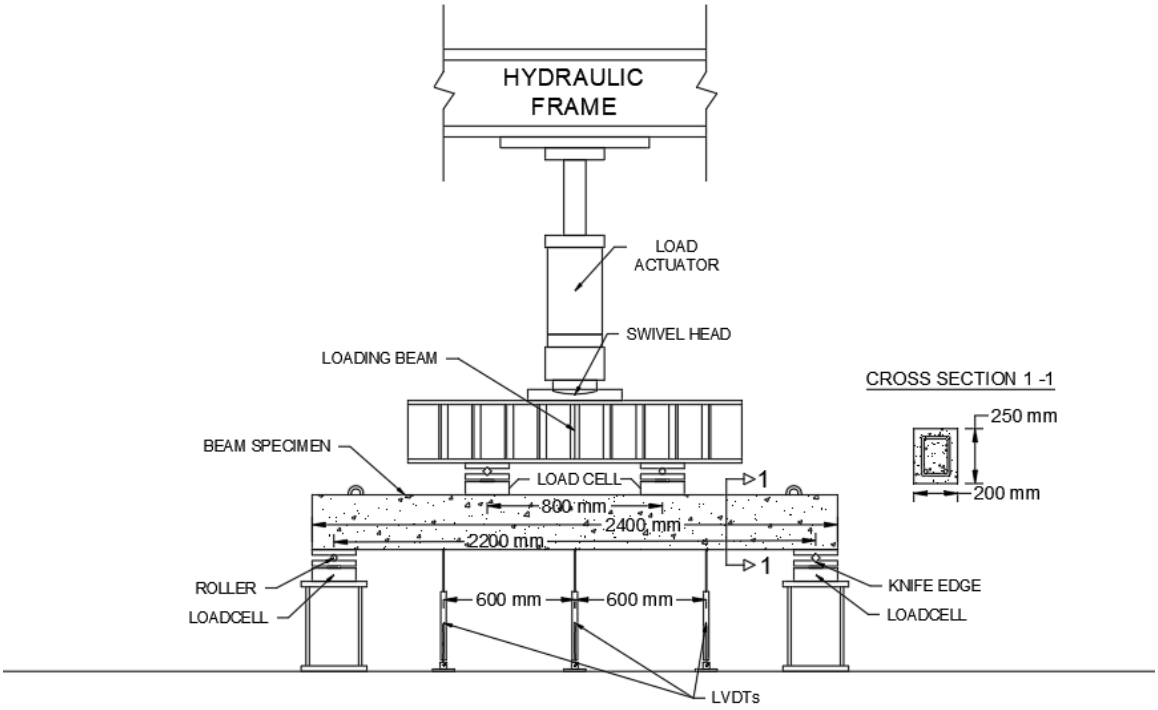

Figure 3.18: Four point bending test setup (Hughes, 2018)

CHAPTER 4
FINITE ELEMENT MODELLING

4.1 General

Finite element (FE) method is a numerical method for obtaining approximate solutions of problems with simple and complex geometries, properties, and loading sequences for which an analytical solution may be difficult to obtain. It represents the full behavior of the structures by dividing them into smaller units (a process known as discretization) interconnected through nodes with each unit having defined physical and mechanical properties (Kachlakev et al. 2001). This process of discretization is critical in developing simplified equations for calculating the behavior of the smaller units and obtaining unknown parameters from the nodes and individual elements. When the equations for each smaller unit have been developed, they are assembled together to find the global equation for the whole structure or system; boundary conditions are also established in this stage. The global equation for the structure is then solved either through direct or iterative methods, after which, additional results of interest from the structure can be obtained (Nikishkov, 2004).

Finite Element softwares incorporate these processes and can be used to model structures with both simple and complex geometries and behaviors. For materials with complex behaviors as observed in this study, proper and accurate finite element (FE) models having a close representation with the experiment was needed to achieve its objective of accurately simulating the behavior of reinforced concrete beams externally strengthened with basalt fiber fabric and predicting its failure modes.

The FE models were developed using commercially available FE software, Abaqus/Explicit (Abaqus, 2018). These models were validated using the test data obtained from 12 tests shown in Table 3.2 (Hughes, 2018). The results of the load-deformation behavior, crack patterns, and failure modes of the test specimens were used to validate the FE models.

4.2 Development of FE Model

The steps involved in the development of each part of the model as well as the interaction and loadings are presented in this section.

4.2.1 Element Selection and Assembly

The assembly of a model is done with the creation of parts which represent each of the individual elements that make up the test specimen and test boundary conditions. Abaqus offers multiple sections in defining each part. Three sections were used for this study which are solid sections, shell sections, and beam sections. These sections could be used for both two- and three-dimensional representations. The parts were modelled as close to the test specimens as possible to ensure that the FE model had a good representation of the test specimens and a high accuracy in the FE results. The parts created for the section include: the concrete beam, the 10M stirrups, 10M longitudinal tension reinforcement, 15M longitudinal tension reinforcement, steel support plates, and the BFRP fabrics. Geometry and dimensions of all the parts were the same as the experiment (Hughes, 2018).

4.2.1.1 Concrete Beams

The concrete beam was modelled using eight-node linear brick (solid) elements with reduced integration (C3D8R). The length of the beam was 2370 mm and the cross-

sectional dimensions were 200 mm x 250 mm (see Figure in 4.1). Brick (solid) elements are recommended for both linear and complex non-linear analyses involving plasticity and large deformations, and since reinforced concrete exhibits such complex non-linear behavior, the C3D8R element was chosen. Elements can be modelled using linear (first-order) or second order (quadratic) elements with full or reduced integration. First order elements use linear approximations to calculate the displacement of a structure and can be used for plane strain problems with reduced integration to prevent mesh locking when the material is incompressible. Linear elements are better for analysis with large mesh distortion. Second order elements, however, use quadratic approximations to calculate the displacement of a structure and are more sensitive and accurate for analysis with bending and stress concentrations. Though second order elements tend to produce more accurate results, they are computationally more expensive than linear elements (Abaqus, 2018).

The reduced integration option minimizes computational time by reducing the integration points required to form the element stiffness matrix; it also reduces shear locking effect. Reduced integration C3D8R was adopted for this study. A mesh convergence study was conducted to determine the optimum mesh size as discussed in Section 4.3. Compressive and tensile properties obtained from the material tests as described in chapter 3 (section 3.2.1 and 3.2.2), as well as the tension and compressive damage behavior of concrete as discussed in section 3.2.3 were included in the model.

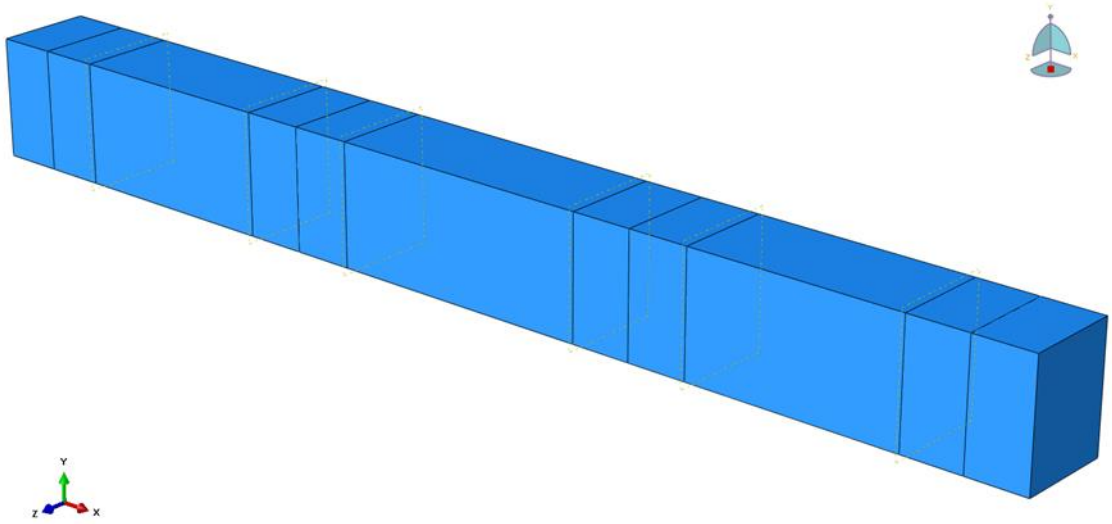

Figure 4.1: 3D Solid beam part

4.2.1.2 Steel Support Plates

The eight-node linear brick (solid) element with reduced integration (C3D8R) was also used to model the steel support plate with cross-sectional area of 200 x 250 mm and thickness of 25 mm. These support steel plates were used as support at the bottom of the concrete beam and also for the load application at the top the beams (see Figure 4.6). The interaction between the steel support plates and the concrete beam was defined and discussed in section 4.3.2. A mesh convergence study was also conducted on the optimum element size for the steel plates.

4.2.1.3 Steel reinforcement

The steel reinforcement rebars which include the stirrups (shear reinforcement), longitudinal tension rebars, and compression rebars were modelled using two-node linear beam element (B31) as shown in Figure 4.2. Steel reinforcement can be modelled in Abaqus using either truss or beam elements. These elements are assigned in the wire region and can be used in two (plane) or three (space) dimensions. Truss elements are

used to model slender structures that have only axial stiffness and no bending stiffness while beam elements are used to model structures that have both axial and bending stiffness and which have a cross-section that is small compared to its length. For this study, the steel rebars were modelled using beam element (B31) because large displacements were expected in the analysis. Truss elements may experience convergence problems in such analyses, beam elements are geometrically simple and can be applied for such analysis (Abaqus, 2018).

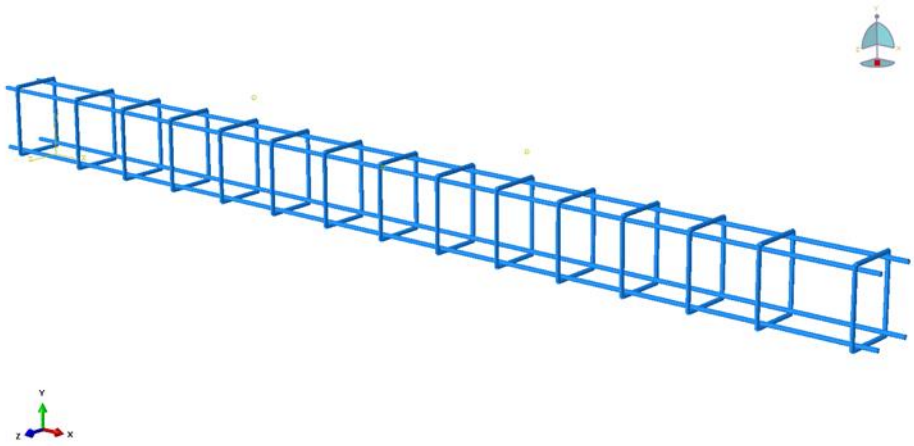

Figure 4.2: Arrangement of steel reinforcement

4.2.1.4 FRP composite

The modelling of the basalt fibre reinforced fabric (BFRP composite) was done using four-node conventional shell element with reduced integration and hourglass control (S4R). The thickness of this element was chosen to be 0.45 mm since each layer of basalt fibre fabric was 0.45 mm. Abaqus provides two options for defining shell elements and these are: conventional shell element and continuum shell element. While conventional shell element is used to model the geometry of the shell as a plane surface and define the thickness in the section property definition, continuum shell element models the shell as a

three-dimensional body and define the thickness from the nodal geometry. Although continuum shell elements look like three-dimensional solid elements, their constitutive and kinematic behavior is similar to the conventional shell elements. Additionally, continuum shell elements have only displacement degree of freedom while conventional shell elements have both displacement and rotational degrees of freedom (Abaqus, 2018). Conventional shell element was adopted in the current study to model BFRP fabrics to ensure that the FE models have both displacement and rotational degrees of freedom.

4.2.2 Material Properties

It is important to define the material properties of each part of the FE model to effectively simulate the behavior of the concrete beam using the FE software Abaqus. The accuracy of the FE model in predicting the behavior and failure modes of the FE model largely depends on the specified material properties. Abaqus provides the option of specifying material properties in both elastic and plastic ranges, including the damage parameters. Strain hardening and strain softening behaviors of concrete are defined using the plastic behavior of each constituent material.

Concrete

Material test was carried out on the concrete cubes and cylinders to determine its properties. Compressive and tensile properties, compressive and tensile damage properties, and fracture energy were obtained from these tests. The material properties of concrete used in the model were obtained from the compressive stress and strain values shown in Figure 3.2 and as shown in Table 4.1.

Table 4.1: Elastic material properties of concrete

E	μ
25400 MPa	0.18

The plastic properties of concrete were defined using concrete damaged plasticity (CDP) model available in Abaqus. This CDP model assumes two failure modes for reinforced concrete, which are compressive crushing and tensile cracking.

Steel reinforcement

Material properties for the steel reinforcement were obtained from the steel coupon tests as specified in chapter 3. Two different steel reinforcement rebars were used and they are 10M rebar (cross-sectional area of 100 mm^2) and 15M rebar (cross-sectional area of 200 mm^2). The behavior of the steel reinforcements in both elastic and plastic ranges were obtained from the tensile stress-strain curve. The elastic properties used for the steel materials are shown in Table 4.2 while the true stress-true plastic strain behavior of the 10M and 15M rebars are shown in Table 4.3 and Figure 4.3.

Table 4.2: Elastic properties of 10M and 15M steel reinforcement

E	μ
201,000 MPa	0.3

The definition of the true stress and strain behavior of the steel reinforcement is required in Abaqus for defining the plastic behavior of both steel and concrete. These were calculated using Equation 4.1 and 4.2, respectively.

$$\sigma_{true} = \sigma_{nom}(1 + \epsilon_{nom}) \quad (4.1)$$

$$\epsilon_{true} = ln(1 + \epsilon_{nom}) \quad (4.2)$$

In these equations, σ_{true} is the true stress, σ_{nom} is the engineering or nominal stress, ϵ_{true} is the true or logarithmic strain, and ϵ_{nom} is the engineering or nominal strain.

Table 4.3: True stress-true plastic strain behavior of 10M and 15M steel rebars

10M		15M	
Stress (MPa)	Strain	Stress (MPa)	Strain
504	0.00000	410	0.00000
509	0.00250	417	0.00585
529	0.00507	424	0.00671
579	0.01218	444	0.01004
603	0.01633	495	0.01999
645	0.02462	521	0.02659
683	0.03404	541	0.03232
709	0.04221	565	0.04046
733	0.05108	578	0.04529
738	0.05342	590	0.05010
753	0.06103	609	0.05889
763	0.06623	625	0.06757
773	0.07328	647	0.08244
791	0.08730	654	0.08786
799	0.09657	670	0.10096
803	0.11370	690	0.12200

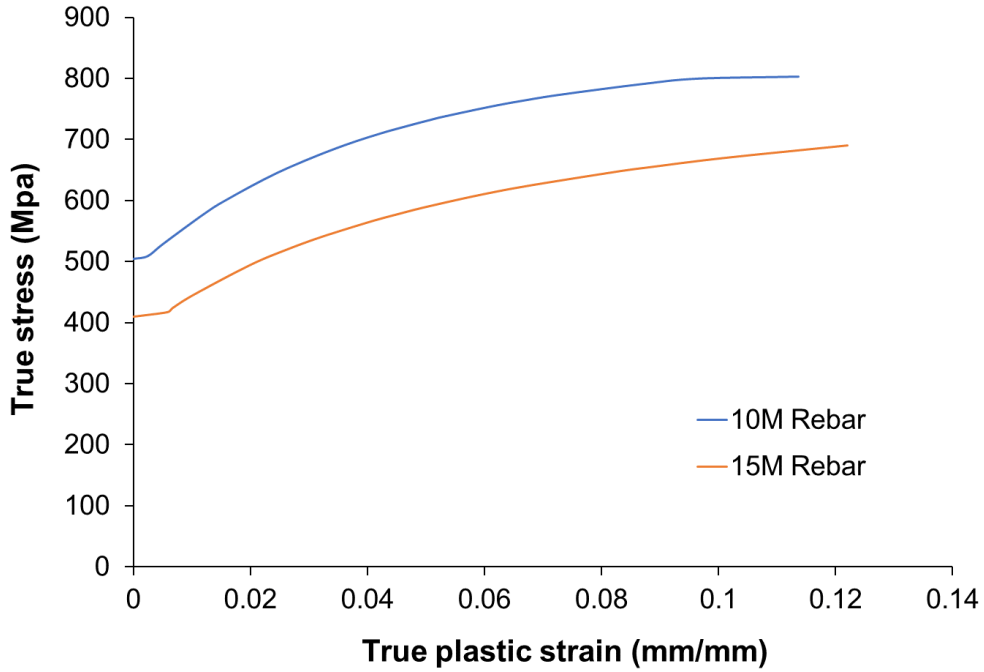

Figure 4.3: True stress- true plastic strain behavior of the steel rebars

BFRP composite

The elastic material properties of the BFRP composite were obtained from the coupon test as specified in the ASTM D3039/D3039-14 (ASTM, 2017b). This test was conducted at the University of Windsor structures laboratory by Hughes (2018) and the results obtained (as shown in Table 4.4) were adopted in the current study. The BRFP was defined in the model as a lamina with a homogenous section as shown in Figure 4.4. Lamina is used in Abaqus to define the material properties of thin-layer structures such as FRP. These material properties include the elastic modulus, shear modulus, and Poisson ratio.

Table 4.4: Elastic material properties of BFRP composite

E1	E2	Nu12	G12	G13	G23
21000	5000	0.44	7000	3000	3000

In Table 4.4, E1 is the elastic modulus in the longitudinal direction of the fibre, E2 is the elastic modulus in the transverse direction of the fibre, Nu12 is Poisson ratio while G12, G13, and G23 are the shear moduli in the three different planes namely 12, 13, and 23. After specifying the material properties, a coordinate system must be adopted to define the material orientation. Three coordinate directions are specified with directions 1, 2, and 3 defined as the longitudinal (x-axis), transverse, and normal directions of the fibers, respectively. The number of layers of the fibers (referred to as plies), the angle of rotation of each ply as well as the thickness of each ply are also specified.

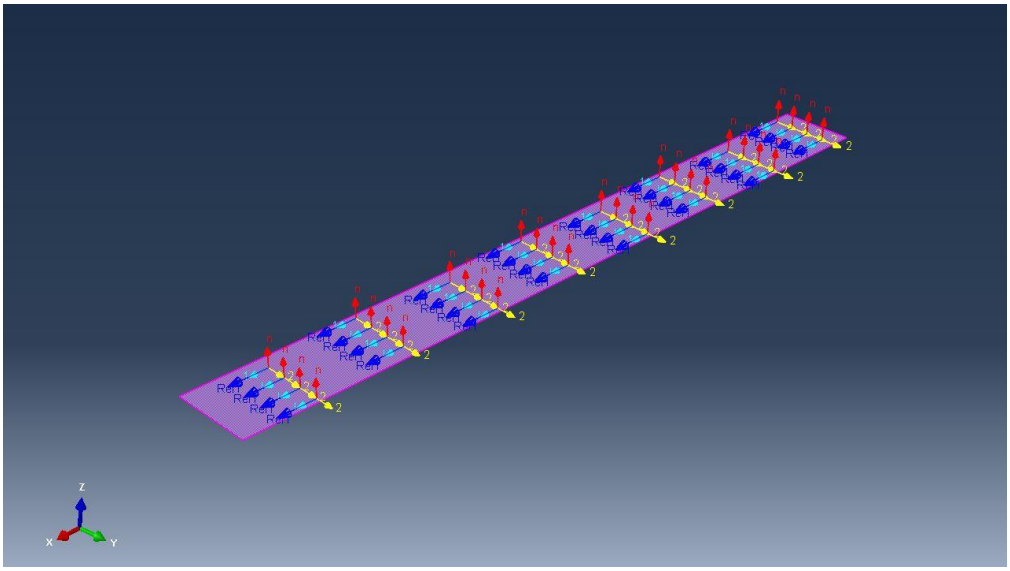

Figure 4.4: BFRP coordinate definition

The failure properties of the fibers are defined in Abaqus using Hashin's criteria (Hashin, 1980) shown in Equations 2.7 to 2.10. Hashin's criteria is a damage theory used to detect the initiation of failure in a composite material. It recognises a failure has occurred when

one of the failure mechanisms relating to the fiber or the matrix has occurred. This failure mechanism includes tensile fiber failure, compression fiber failure, tension matrix failure and compressive matrix failure as discussed earlier in section 2.6.1. The evolution of the failure is defined by specifying the fracture energy released by the fibers and is calculated as shown in Equations 4.3 and 4.4.

$$G_c = \frac{l^* \sigma_u \varepsilon_u}{2} \qquad (4.3)$$

$$l^* = \frac{mesh\ size + fiber\ thickness}{2} \qquad (4.4)$$

In Equation 4.3, G_c is the fracture energy, l^* is the characteristic length and is calculated using Equation 4.4, σ_u is the ultimate stress of the fiber, and ε_u is the ultimate strain of the fiber.

4.2.3 Interaction

Interaction between the various parts in Abaqus is done through the interaction module. Abaqus offers several options to define how the solid and shell parts are connected. Three interactions were defined for the FE model and they are tie constraints, embedded rebars, and surface-to-surface contact. The interaction between the concrete and steel supports plates was modelled using both tie constraints and surface-to-surface contact to compare the differences in behavior when these two modelling techniques are used. Both interaction definitions require that the specification of a master and slave surface before the analysis. Materials with higher stiffness are selected as the master surface while those with less material stiffness are selected as the slave surface. Hence, concrete was chosen as the slave surface due to its weaker material stiffness while the steel support was chosen as the master slave surface. For the surface to surface contact, the definition of a

friction coefficient between the interacting surfaces, that is, steel plate and concrete is required in for the representation of the tangential behavior of the contact. Frictional coefficient of 0.57 between concrete and steel, as recommended by Rabbat and Russell (1985), was adopted for this study. The load-deflection response of the model using both interaction constraints were compared, and apart from the noise observed for the surface-to-surface contact interaction, the results indicated that both interaction constraints produced identical values and predicted the beam behavior accurately (see Figure 4.5). Although surface-to-surface contact is a better representation of the experimental test setup, due to its high computational cost in running the analysis and the noise observed in its results, tie constraint was adopted in the current study.

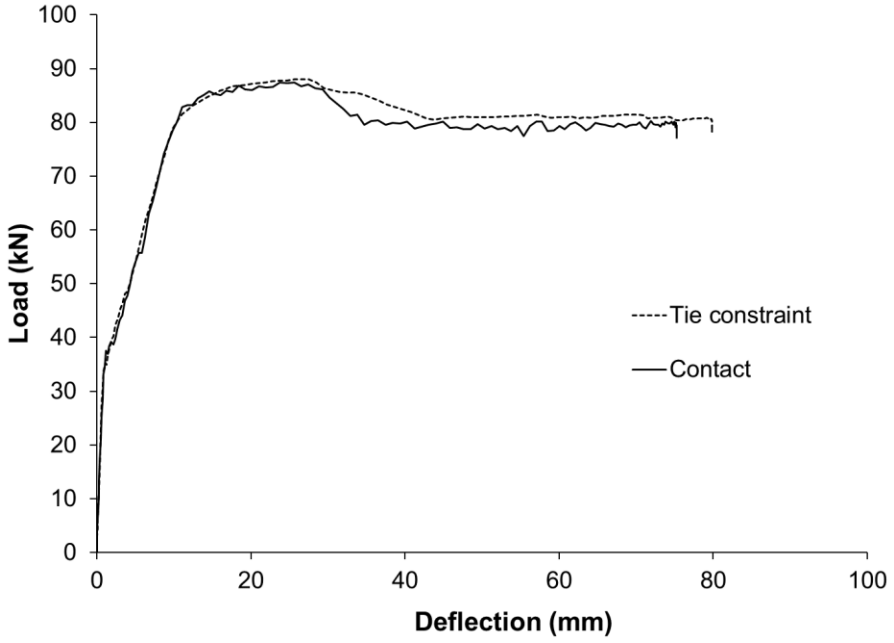

Figure 4.5: Load-deflection behaviour using tie constraint and contact interaction

Embedded regions constraint was selected to define the interaction between concrete and all the steel reinforcements (stirrups, compression, and tension rebars). The steel reinforcement was selected as the embedded element while the concrete part was selected

as the host element. This constraint ensures that the degrees of freedom of the nodes of the embedded element become constrained to the degree of freedom of the host element. The arrangement of the embedded and host element was representative of the full-sized concrete beam.

The interaction between the concrete beam and BFRP composite was defined using a tie constraint. This interaction assumes a perfect bond between the parts and was used because there was no observed debonding of the BFRP composite from the concrete beam in the tests.

4.2.4 Loading and boundary conditions

Following the definition of the interaction of the various parts of the model, and the material properties, the loads and boundary conditions were defined. The boundary conditions were set as pin and roller supports, similar to the test specimens. The roller support was restrained in translation and rotation in the y- and z- axes (see Figure 4.1 for the axis), while the pin support allowed only rotation about the x-axis. Since the loading was applied to the test specimens using a displacement-controlled setup, a displacement boundary condition was adopted in the model to apply the load. Node sets were created for the loads and support and a displacement of 60 mm on the y-axis was applied to the top beam supports.

4.3 Mesh Convergence Study

A mesh convergence study was conducted to determine the mesh size which provides the most accurate results with optimum computing resources needed for the analysis. This refers to the selection of the mesh (element) size where the results converge. Kachlakev et al. (2001) defined this point of convergence as the point where any further increase in

the mesh density has an insignificant influence on the results. Table 4.5 and Figure 4.6 presents the results obtained with eight element sizes for what concrete: 75, 50, 35, 30, 25, 20, 15, 10 mm and the time taken to complete each of the analysis using a Windows 10 computer with intel core i7-8700 CPU with a processor speed of 3.20GHz and 15.8 usable RAM.

Table 4.5: Mesh convergence table

Element size (mm)	10	15	20	25	30	35	50	75
Stress (MPa)	35.3	34.8	33.8	33.2	32.9	31.7	27.8	14.8
Number of elements	125000	38798	15600	7840	6020	3108	1080	324
Time (s)	7735.2	2870.7	1454.2	780.7	660.0	494.7	299.3	223.1

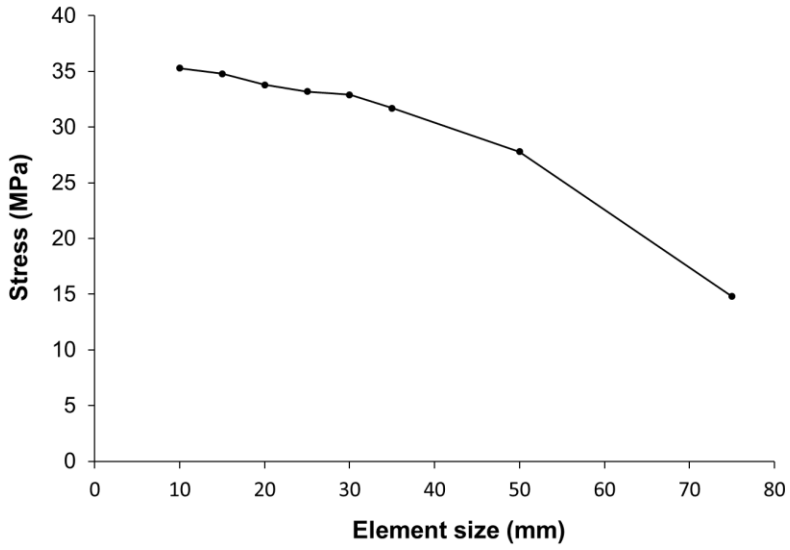

Figure 4.6: Mesh convergence study for the concrete beam

The control beam with 0.75% flexural reinforcement ratio was used to conduct the convergence study and only the mesh density for the concrete beam was considered. The mesh convergence study was based on the value of the maximum stress obtained at the

mid-span of the concrete beam. The study showed that there was no significant change between the mesh size 35 mm and size 10 mm in terms of the maximum stress in the concrete which was found to 35 MPa (shown in section 5.1.1). This is understandable because the interaction between the concrete and rebars was defined effectively through the introduction of tension stiffening into the model. The introduction of tension stiffening into the model reduces mesh dependency of the result (Abaqus, 2018). Element size of 20 mm was adopted for the steel and concrete beam parts for the analysis (shown in Figure 4.7) as any further reduction in the element size led to an increase in the computational time for the analysis.

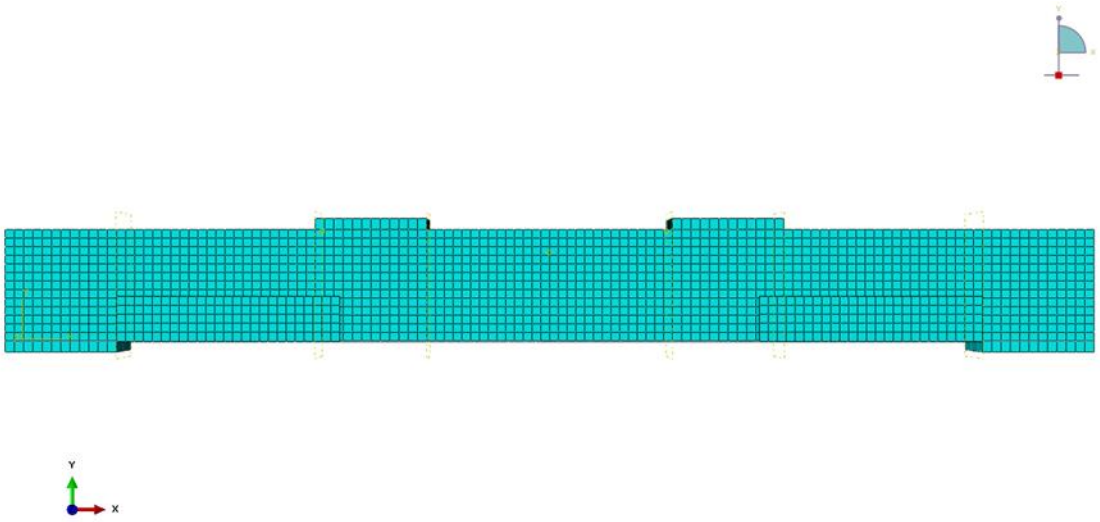

Figure 4.7: Beam mesh

4.4 Summary

FE study was conducted on twelve beams using the commercial software Abaqus to understand and predict the behavior of the reinforced concrete beam strengthened with BFRP fabrics. The dimension, loads and boundary conditions were kept as close to the

experiment as possible. The results of the experiments in Phase 1 and Phase 2 as well as the results of the FE model will be discussed in detail in the next chapter.

CHAPTER 5
RESULTS AND DISCUSSION

This chapter presents and discusses the result of the material testing used to develop the finite element (FE) models. The material test results were obtained from the three different materials tests: the concrete substrate, the steel reinforcement, and the basalt fibre reinforced polymer (BFRP) fabrics. This chapter also discusses the results obtained from the FE models of the twelve reinforced concrete beams and compared with the data obtained from the full-scale tests conducted by Hughes (2018). In addition, a parametric study was undertaken to determine the optimum number of layers of basalt fiber fabrics required for a target level of strength improvement of the beams.

5.1 Material properties

The material properties obtained from the experimental tests used for the calibration of the finite element model are presented and discussed below in this section.

5.1.1 Compressive test

Compressive strengths were obtained from the concrete cylinders according to ASTM standard C39/C39M (ASTM 2018b) after the concrete achieved its 28-day strength. Monotonically increasing axial load was applied to each concrete cylinder until it failed due to crushing. Table 5.1 shows the summary of the results.

Table 5.1: Compressive strength results

Number of cylinders	Compressive strength (MPa)	Coefficient of variation (%)
3	35	8.9%

5.1.2 Compressive Cyclic test

The results obtained from the monotonic compressive test and cyclic compressive tests conducted on the concrete cylindrical specimens provided stress-strain behaviors in both elastic and plastic ranges. The hardening and softening regions of the stress-strain curve were implemented in the Abaqus models (Abaqus, 2018) in terms of inelastic strain as calculated by the Equation 5.1.

$$\varepsilon_{in} = \varepsilon_t - \varepsilon_{el} \tag{5.1}$$

Where, ε_{in}, ε_t and ε_{el} are the inelastic strain, total strain and elastic strain respectively.

The unloading and reloading data from the cyclic test show the degradation of the elastic modulus of the concrete cylinder and these test data was used to calculate the compressive damage parameter (d_c) as shown in Equation 3.1. Table 5.2 and Figure 5.1 show an example of the summary of the results obtained from the test.

Table 5.2: Yield stress-compressive damage parameter (d_c) values

Yield stress (MPa)	Compressive damage parameter (d_c)
34.91	0
13.94	0.21952
7.25	0.47613
4.70	0.59413
3.31	0.62076

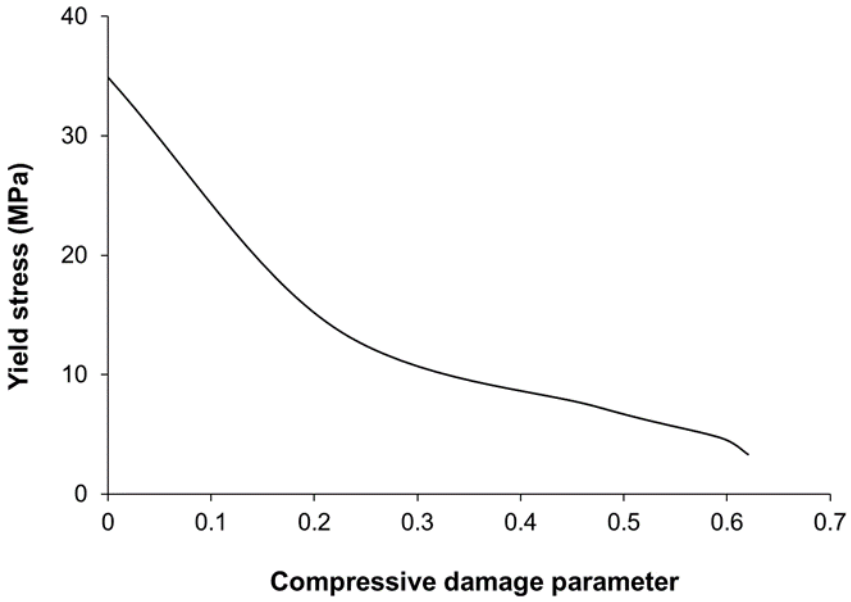

Figure 5.1: Post-yield concrete compressive damage (d_c) behavior

5.1.3 Wedge Split test

Three concrete cube specimens (WST 1-3 in Figure 5.2) with dimensions as given in sections 3.2.3.1 were tested to obtain the load–crack mouth opening displacement (CMOD) curve as shown in Figure 5.2. The results were then subjected to data-reduction and inverse analysis done in MATLAB (MATLAB 2014) using the iterative crack hinge model algorithm developed by Østergaard et al. (2003). The inverse analysis involves an optimization process to obtain the stress-crack mouth opening (σ-w) softening curve of concrete as described by Sousa and Gettu (2006). The stress is then normalized with the tensile strength to obtain the normalised stress-crack mouth opening displacement (σ/f_t-w) curve shown in Figure 5.3 which represents the softening behavior of concrete in tension. This bi-linear curve is a two-phase curve showing the initial and final softening phases of concrete subjected to tension. The normalised stress is then converted to the tension damage parameter (d_t) using Equation 5.2 to obtain the tension damage–CMOD

(d_t-w) behavior as shown in Figure 5.4. The results obtained were used to specify tension damage in the FE model. Crack initiation and propagation in the FE model depends on the accuracy of the test results.

$$d_t = 1 - (\frac{\sigma}{f_t}) \tag{5.2}$$

Where, d_t is the tension damage parameter, σ is the stress in specimen, and f_t is the tensile strength of the concrete.

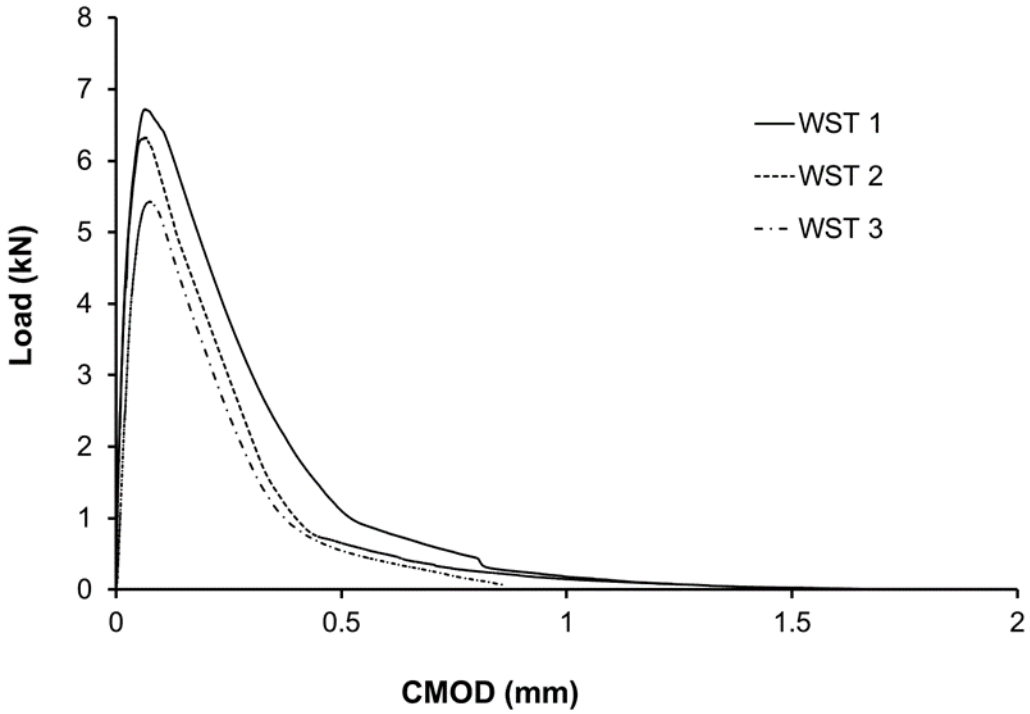

Figure 5.2: Load-crack mouth opening displacement (CMOD) curve

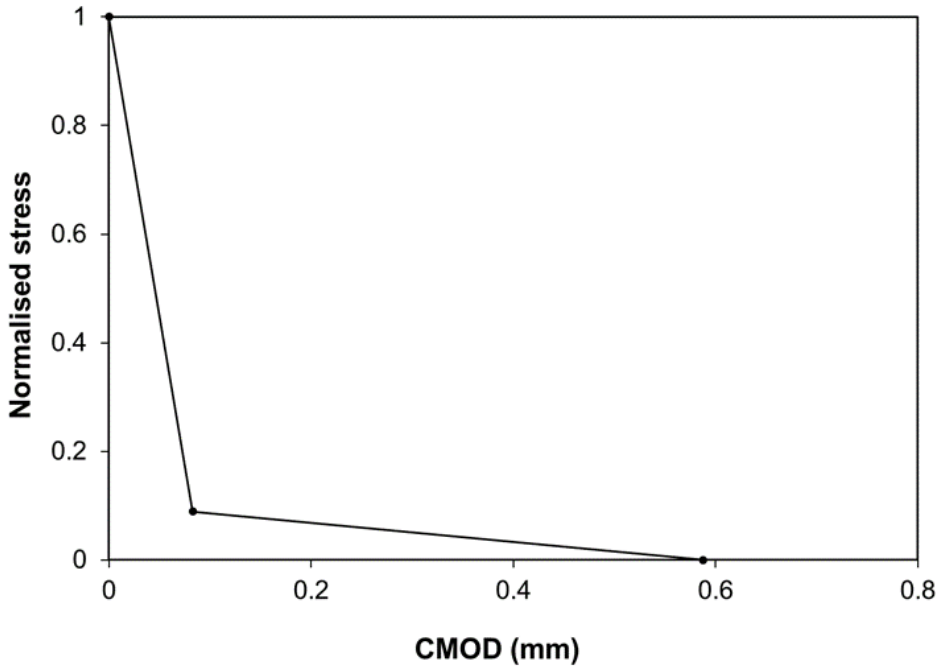

Figure 5.3: Normalised stress-crack mouth opening displacement (CMOD) curve

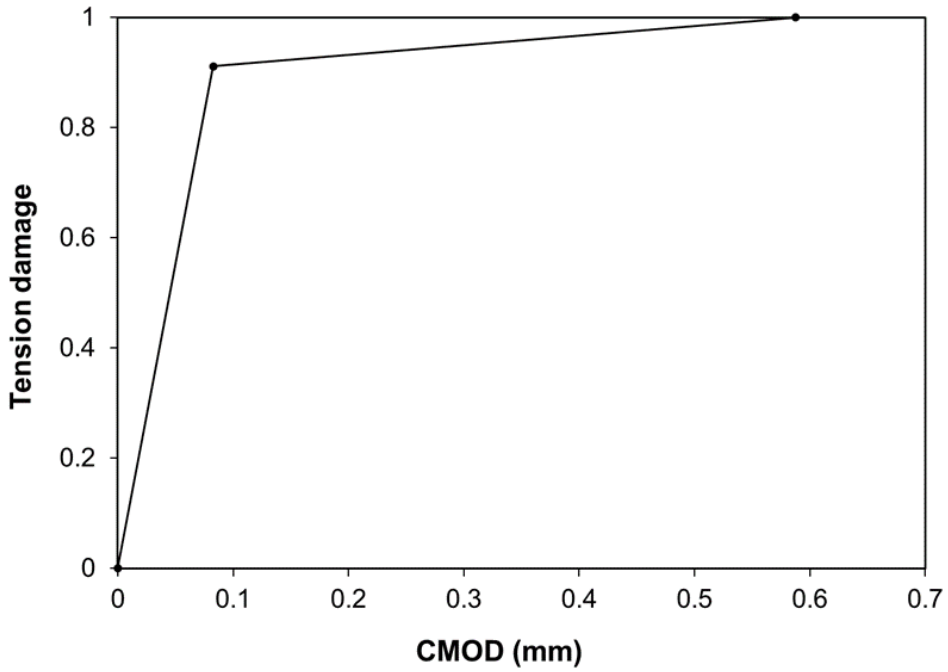

Figure 5.4: Tension damage-crack opening displacement (d_t -w) curve

5.1.4 Three Point Bending test

Three rectangular specimens as discussed in chapter 3 were tested to obtain the fracture energy. The area (denoted as W in Figure 5.5) under the load–crack mouth opening displacement (CMOD) curve presented in Figure 5.5. is calculated using Riemann sum as shown in Equation 5.3. This area was then used to obtain the fracture energy as shown in Equation 3.4.

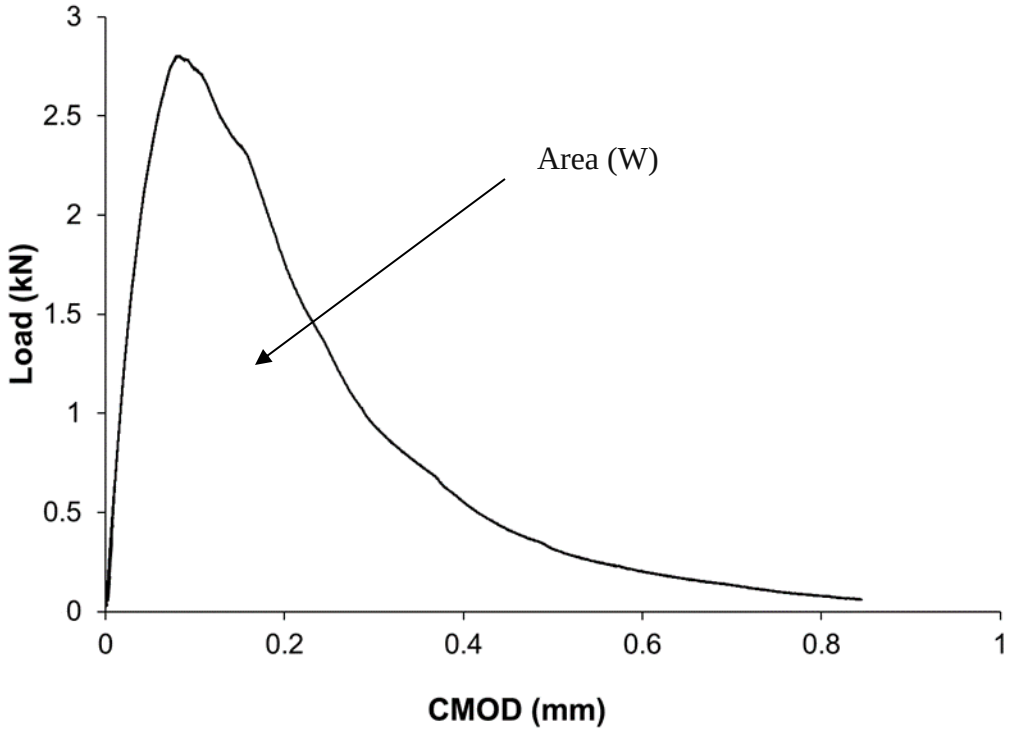

Figure 5.5: Load - CMOD curve for the three-point bending (TPB) test

$$W = \sum_{i=1}^{n} \left[(\Delta_{i+n} - \Delta_i) * \frac{f_i + f_{i+n}}{2} \right] \tag{5.3}$$

The value of the fracture energy as shown in Table 5.3 is important in representing the behavior of concrete beams in tension.

Table 5.3: Fracture energy obtained from three-point bending tests

Number of specimens	Fracture energy (N/mm)	Coefficient of variation (%)
3	0.091	6.9%

5.2 Load-deflection behavior

This section discusses the load-deflection behaviors of the control and strengthened beams obtained from the FE analyses. The comparison between the results of the test specimens and the finite element (FE) models are also discussed.

5.2.1 Control beams

Figures 5.6 to 5.8 show the load-deflection behaviors of the control beams (beams without any basalt fibre fabric) obtained from the tests conducted by Hughes (2018) and the results obtained from the finite element analysis (FEA). The ultimate load of the test specimen and FE model is represented by U in the figures. The load and deflection values for the test specimen were obtained from the loading actuator and linear variable displacement transducer (LVDT), respectively. The LVDT was placed at the underneath surface of the beam at its mid-span to obtain the deflection at the various loads. The deflections of the FE models were obtained at the same point as the test specimens. As can be found from Figures 5.6 to 5.8, there is a good correlation between the test results and the FE models at both elastic and plastic regions. The maximum percentage difference in the ultimate load and deflection at the ultimate load values for the tests and FE models for the control specimens is 2.35% and 18.5%, respectively as shown in Tables 5.4 to 5.6. In general, a stiffer slope in the linear part of the load-deflection behaviors was observed for the FE models. This is due to a higher cracking load predicted by the FE model. This observation is in line with the earlier studies where

carbon, glass, and green natural fibers were used (Cervantes et al. 2014; Hawileh et al. 2013; Ibrahim and Mahmood 2009; Said et al. 2016). The increase in stiffness could be attributed to the fact that the FE model assumes an ideal condition and a perfect bond between the concrete and steel rebars. As well, FE models do not take into considerations defects such as presence of micro-cracks formed when drying shrinkage occurs in the concrete.

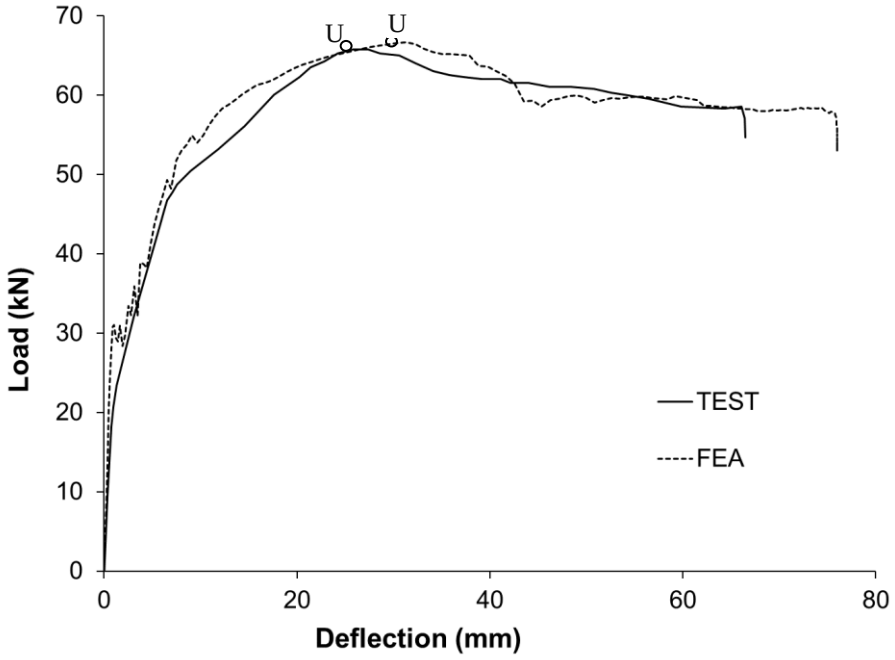

Figure 5. 6: Load-deflection behavior of control beam 0.5RR

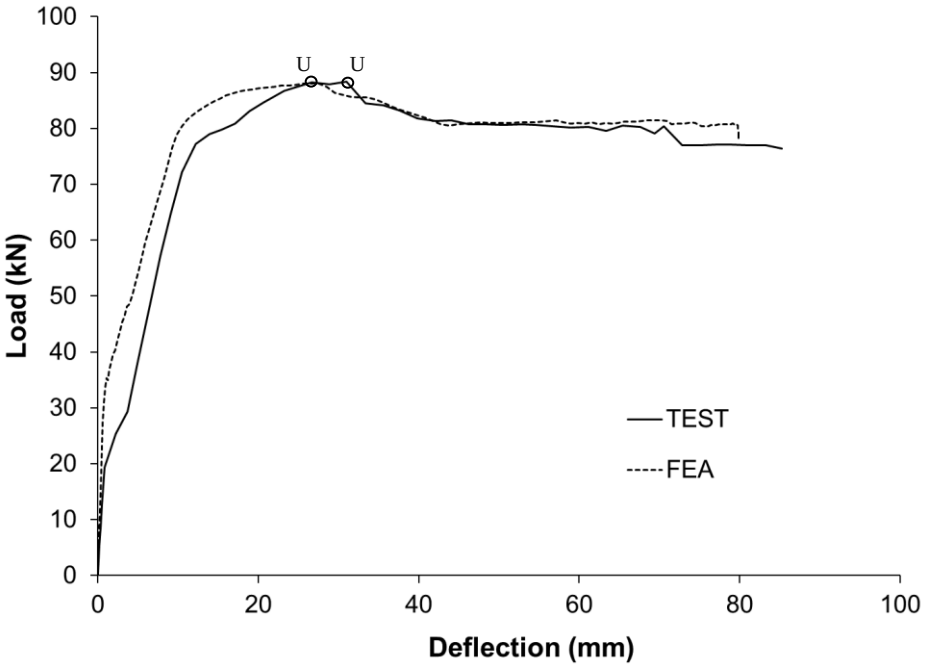

Figure 5. 7: Load-deflection behavior of control beam 0.75RR

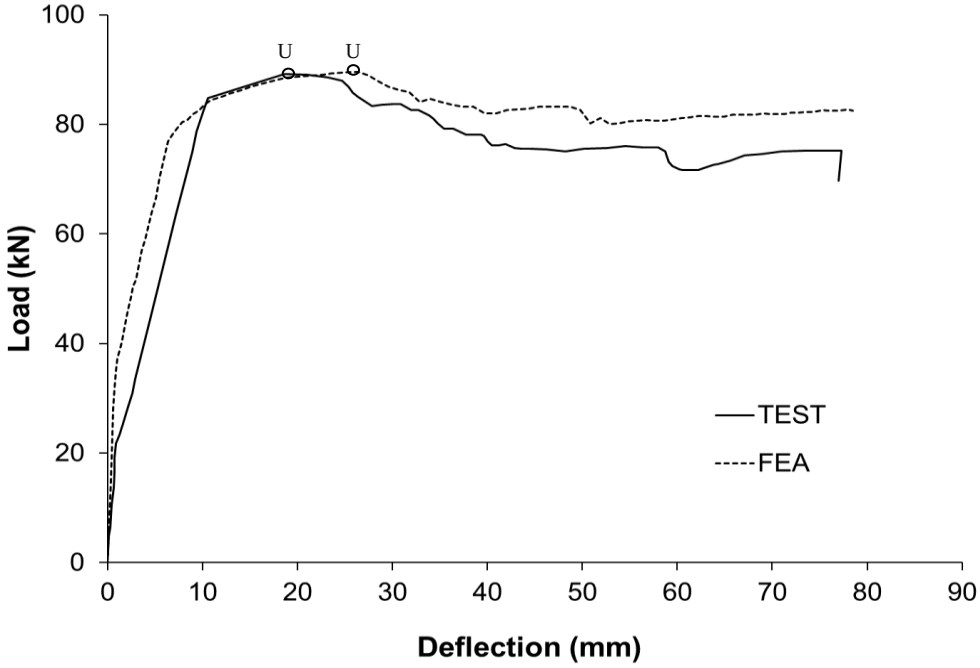

Figure 5.8: Load-deflection behavior of control beam 1RR

Table 5.4: Load and deflection results for 0.5RR control beam

	Control Beam 0.5RR		
	Test (kN)	FEA (kN)	Difference (%)
Cracking Load	27	30	11.1
Ultimate Load	66	67	1.51
Deflection at ultimate load	27	32	18.5

Table 5.5: Load and deflection results for control beam 0.75RR

	Control Beam 0.75RR		
	Test (kN)	FEA (kN)	Difference (%)
Cracking Load	27	32	18.5
Ultimate Load	89	87	-2.2
Deflection at ultimate load	27	24	-11.1

Note: Negative sign means that the FE model predicted a lower value than the test value.

Table 5.6: Load and deflection results for control beam 1RR

	Control Beam 1RR		
	Test (kN)	FEA (kN)	Difference (%)
Cracking Load	28	33	17.9
Ultimate Load	85	87	2.35
Deflection at ultimate load	24	29	20.8

5.2.2 Strengthened beams

The load-deflection behaviors of the concrete beams strengthened with different numbers of layers of basalt fibre fabrics are discussed in this section.

Figures 5.9 to 5.11 compare the load-deflection behaviors obtained from the tests with the load-deflection behaviors obtained from FE analysis (FEA) of the strengthened beam with flexural reinforcemnet ratio of 0.5%. The ultimate load of the test specimen and FE model is represented by U in the figures. It was found that the results obtained from FE models correlate well with the test results. At the linear phase (prior to cracking), the FE models and the test data have almost the same stiffness with slightly different cracking loads. In general, the cracking loads predicted from the FE models are slightly higher than the cracking load predicted by the tests. This may be due to the presence of defects in test specimens as discussed in section 5.2.1.

For the beams strengthened with two layers of basalt fibre fabric (Figure 5.9), the FE model predicted the ultimate load which is 5.3% less than that of the ultimate load exhibited by the test specimen. The FE model predicted the deflection at ultimate load which is 8 mm less than the test specimen exhibited. Although the failure modes were the same with fiber-rupture occurring for both FE model and test specimen, the FE model experienced the rupture all at once while for the test specimen rupture was a gradual progression.

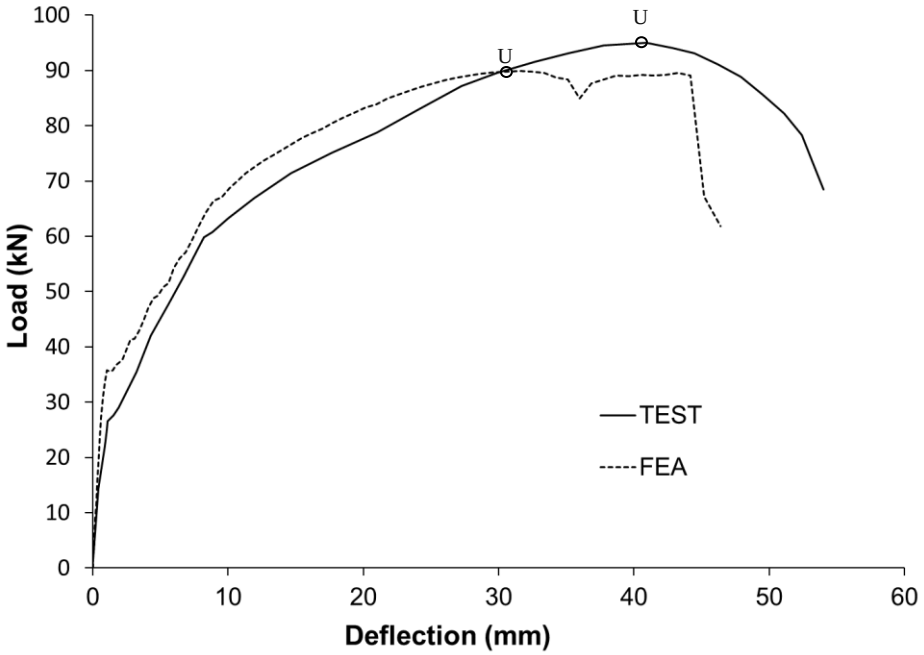

Figure 5.9: Load-deflection behavior of strengthened beam 0.5RR-2L

For the beam strengthened with four layers of basalt fibre fabric, the FE model predicted the ultimate load which is 3.1% less than that exhibited by the test specimen. However, for the value of deflection, the FE model predicted the deflection at ultimate load is 60 mm which is 7 mm higher than that predicted by the test specimen (Figure 5.10). The reason for this difference is discussed in section 5.4 (failure modes).

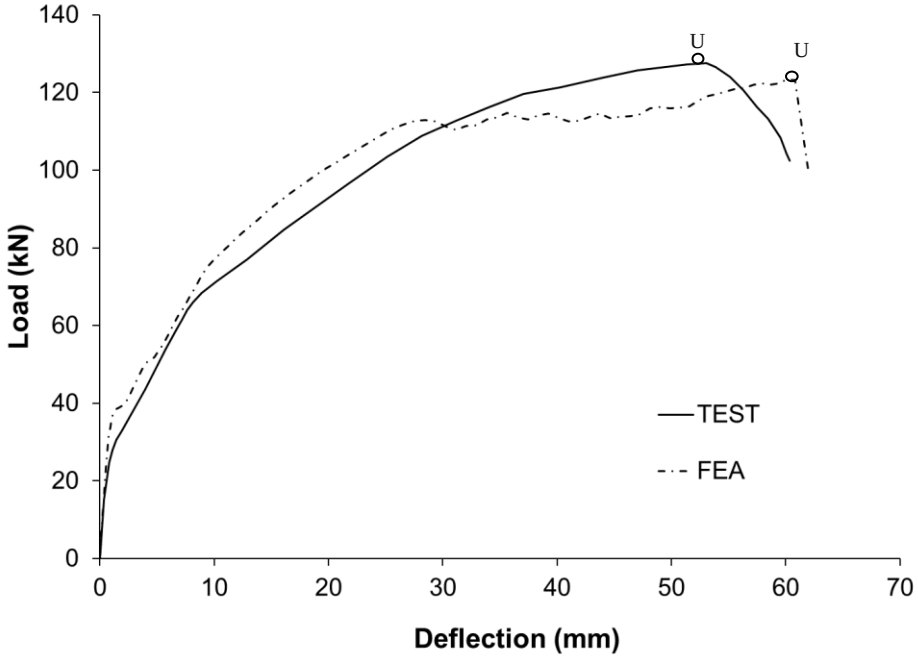

Figure 5.10: Load-deflection behavior of strengthened beam 0.5RR-4L

For the beams with eight layers of basalt fibre fabric, the FE model predicted a 4.2% higher ultimate load and a 6 mm higher deflection at ultimate load compared to the test specimen (Figure 5.11). The failure modes observed for all the strengthened beams in the test was due to steel yielding followed by concrete crushing and followed by the fiber rupture except for beams with eight layers of basalt fibers. For the beam strengthened with eight layers of fabric, a sudden failure at 26 mm mid-span deflection was observed in the test specimen while the failure of the FE model occurred at a later deflection of 32 mm.

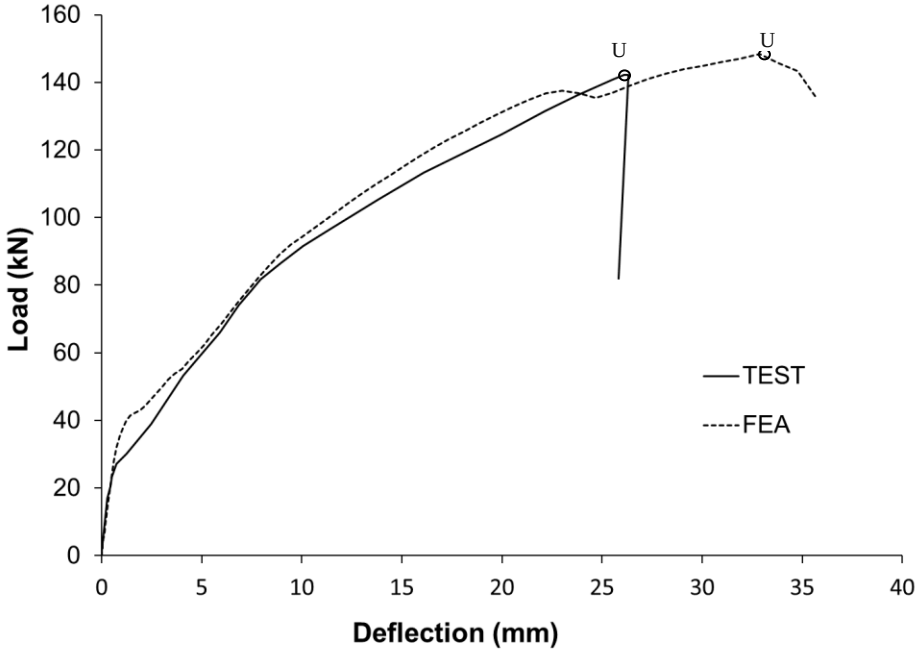

Figure 5.11: Load-deflection behavior of strengthened beam 0.5RR-8L

Figures 5.12 to 5.14 show the load-deflection responses of the strengthened beams which had flexural reinforcement ratio of 0.75% (0.75RR). The ultimate load of the test specimen and FE model is represented by U in the figures. These figures show that there is a good correlation between the FE models and the test specimens when the ultimate load of the beams is compared. The FE models have a similar stiffness at the linear phase of the behavior though the cracking load predicted by FE model is slightly higher that the test specimen exhibited.

For the beam strengthened with two layers of basalt fibre fabric (Figure 5.12), the ultimate load obtained from the test specimen was 112 kN while the FE model predicted an ultimate load of 108 kN. Hence, the FE model predicted 3.6% less in the ultimate load. This variation is not unexpected especially for concrete which is a non-homogenous

material with a non-linear behaviour. The FE model also predicted the deflection at ultimate load which is 13 mm larger than the test specimen exhibited.

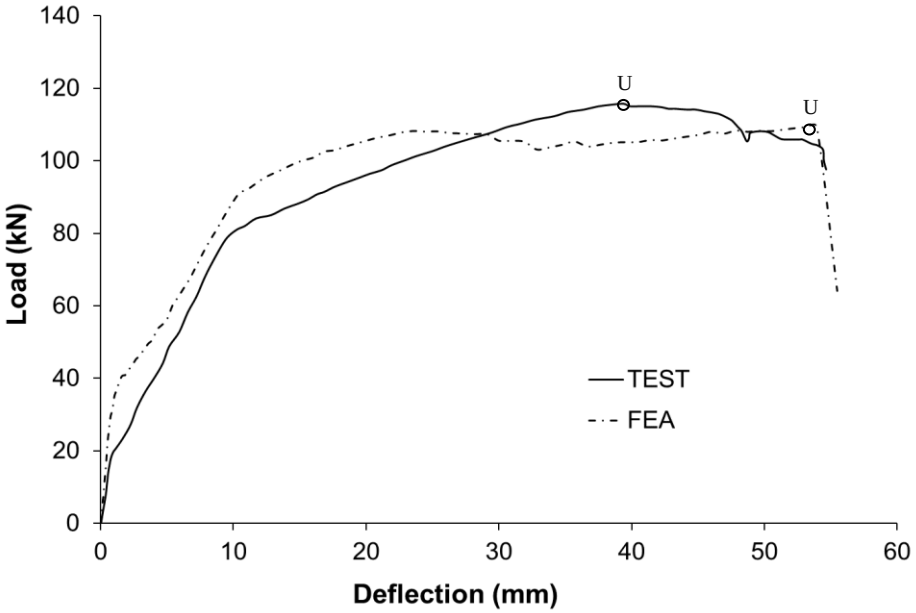

Figure 5.12: Load-deflection behavior of strengthened beam 0.75RR-2L

For the beam with four layers of basalt fibre fabric, the FE model predicted a 1.52% increase in the ultimate load and an 11 mm increase in the deflection at the ultimate load compared to the test specimen (Figure 5.13).

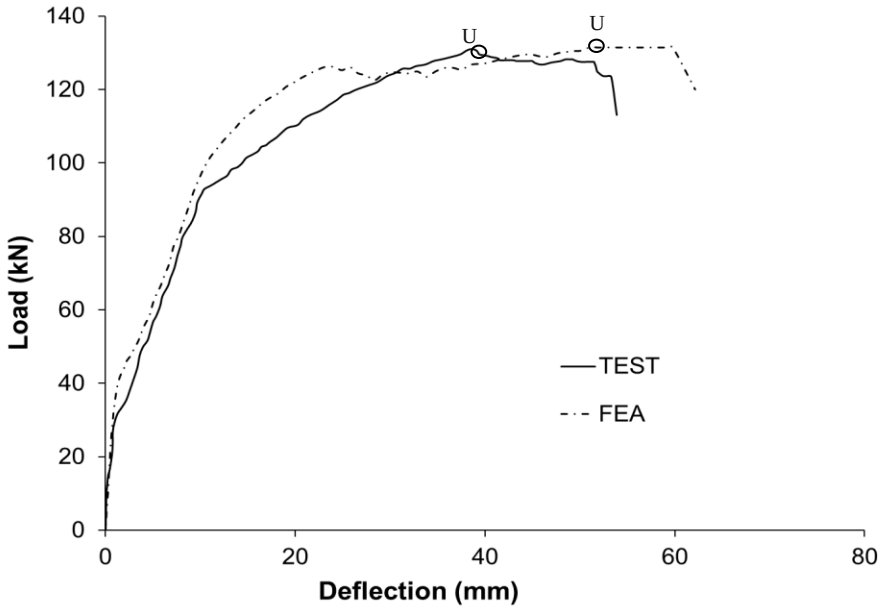

Figure 5.13: Load-deflection behavior of strengthened beam 0.75RR-4L

For beam strengthened with eight layers of fabric, the FE model (Figure 5.14) predicted the ultimate load which is 3.8% less than the ultimate load shown by the test specimen. However, the FE model predicted 5 mm larger mid-span deflection at the ultimate load when compared to the test specimen. In general, the results obtained from the FE models show a good correlation with the tests.

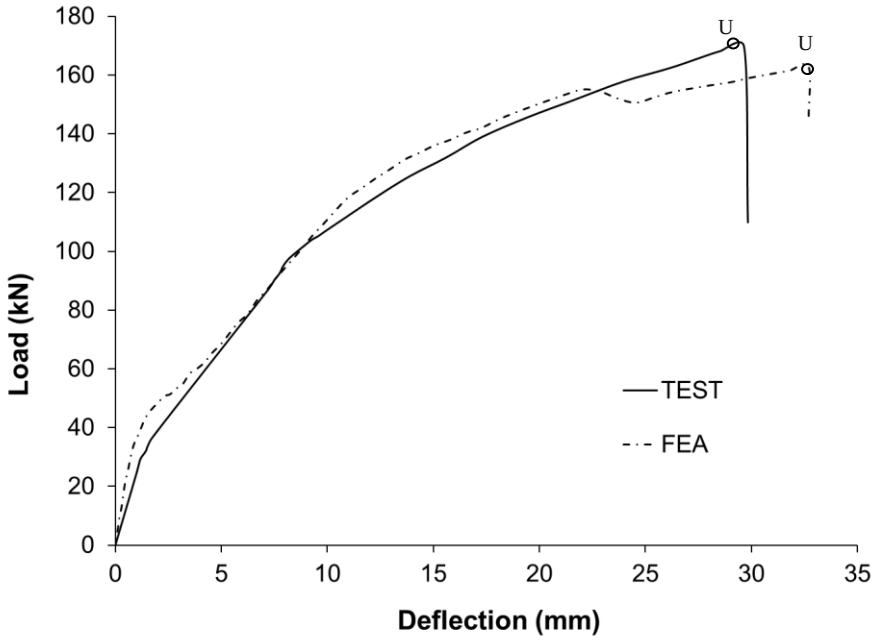

Figure 5.14: Load-deflection behavior of strengthened beam 0.75RR-8L

Figures 5.15 to 5.17 show the load-deflection responses for the strengthened beams having a flexural reinforcement ratio of 1% (1RR). The ultimate load of the test specimen and FE model is represented by U in these figures. As can be found from these figures, there is a good correlation between the FE models and the test specimens when the ultimate load of the beams and the initial stiffness are compared. The FE models of the strengthened beams experienced a higher cracking load than the cracking loads observed in the test specimens. For the beam strengthened with four layers of basalt fibre fabric, the ultimate load of the test and the FE model were found to be 121 kN and 130 kN, respectively. Hence, the FE model predicted the ultimate load which is a 7.4% higher than the test specimen. The deflection at this load was 46 mm and 56 mm for the test specimen and FE model, respectively. Hence, the FE model predicted 10 mm higher deflection value.

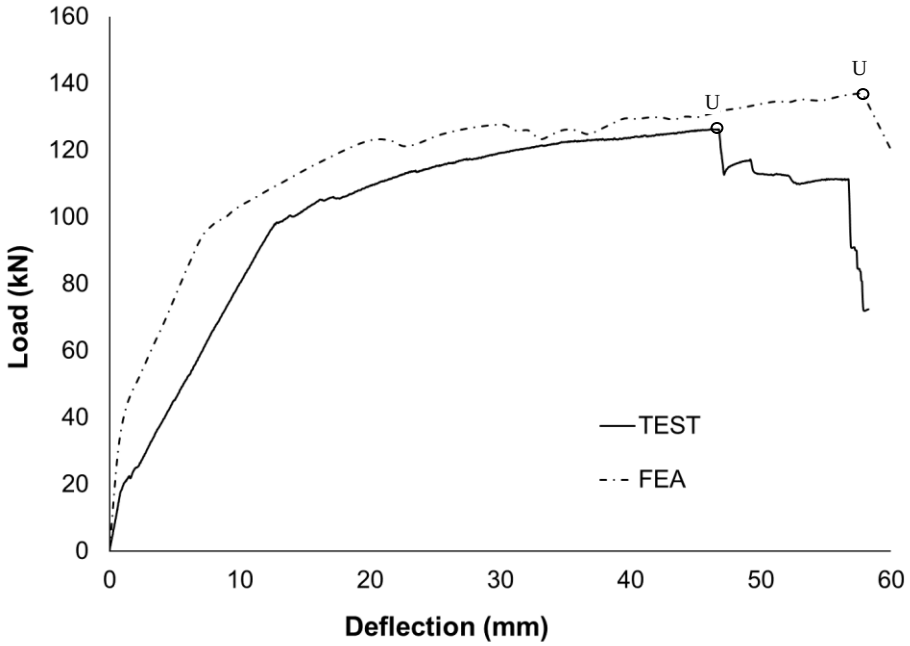

Figure 5.15: Load-deflection behavior of strengthened beam 1RR-4L

For the beam with six layers of basalt fibre fabric, the ultimate loads for the test and FE model were 150 kN and 146 kN, respectively (Figure 5.16). Thus, the FE model predicted a 2.7% less for the ultimate load capacity than that exhibited by the test specimen. The deflection values at the ultimate load were 34 mm for the test specimen and 33 mm for the FE model.

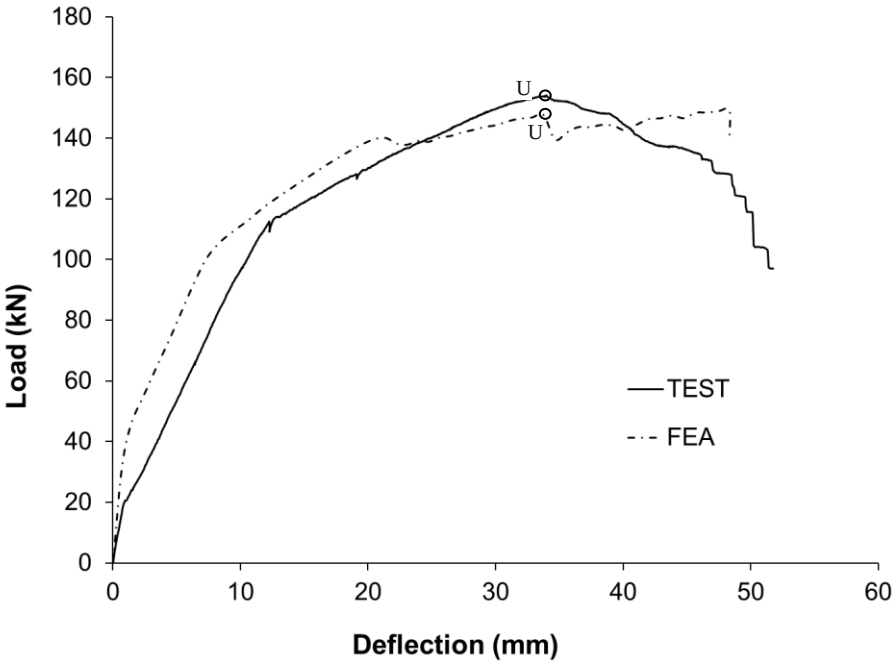

Figure 5.16: Load-deflection behavior of strengthened beam 1RR-6L

The beam with eight layers of basalt fabric attained an ultimate load of 160 kN and 158 kN for the test specimen and the FE model, respectively (Figure 5.17). Hence, the prediction of the FE model for the ultimate load was 1.25% less than the test specimen. The deflection at the ultimate load were 30.9 mm and 29 mm for the test specimen and FE model, respectively. Hence, the results obtained from the FE models with one percent flexural reinforcement ratio are in good agreement with the test results.

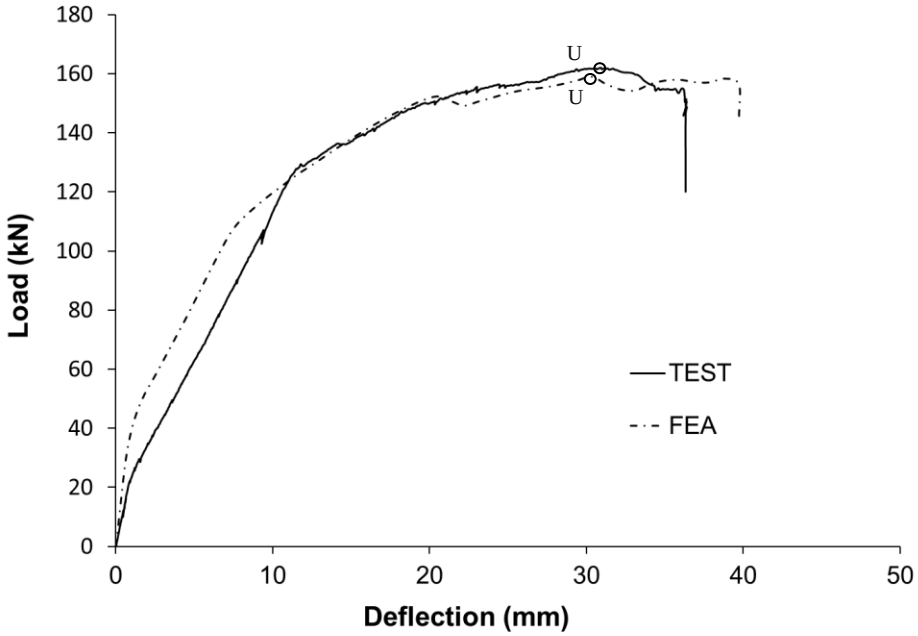

Figure 5.17: Load-deflection behavior of strengthened beam 1RR-8L

From the load-deflection results obtained from the FE models (Figures 5.9-5.17), it can be observed that the external strengthening of reinforced concrete beams with basalt fiber fabric improves the ultimate load capacity in the range of 32% to 120%. The deflections at the ultimate load also improved in the range of 37% to 210% as can be found from these figures and Tables 5.7. Although the FE models were stiffer in the linear phase and predicted a higher cracking load, the value of the ultimate loads showed a good agreement with the test results

5.3 Ductility index

Ductility is the measure of the deformation ability of a structure or structural component before it fails. Ductility is an important measure for reinforced concrete beams when subject to flexural loading as it shows how much energy the beam can absorb before it fails. The ductility of beam can be calculated using the deflection ductility index as

shown in Equation 5.3 which was used by previous researchers (Jayasuriya et al., 2018; Tomlinson and Fam, 2015; Yuan et al., 2013). The results obtained from the FE models and test specimens for the control and strengthened beams are shown in Table 5.7.

$$\mu_{\Delta} = \frac{\Delta_u}{\Delta_y} \tag{5.3}$$

In the above equation, μ_{Δ} is the displacement ductility index, Δ_u and Δ_y are deflection values at the ultimate load and yield load, respectively.

Table 5.7 indicates that the reinforced concrete beam strengthened using basalt fiber fabric can improve the ductility. The ductility of the beams decreased as the amount of flexural reinforcement increased and this observation agrees with the previous study conducted by Rao et al. (2007). The beams with flexural reinforcement ratio of 0.5% (specimen 0.5RR) exhibited the highest ductility of the three reinforcement ratios (0.5%, 0.75%, and 1%) and both the test specimens and the FE models showed the same trend. The beams with the highest flexural reinforcement ratio (1%) or (specimen 1RR) showed the lowest ductility values among the beams built with three different reinforcement ratios. The maximum ductility of specimen 0.5RR (beam with flexural reinforcement ratio of 0.5%) was 15.9 and 11.8 obtained from the test and FE model, respectively. For specimen 0.75RR (beam with flexural reinforcement ratio of 0.75%), the maximum ductility value of 9.3 was obtained from the test and 9.0 obtained from FE model. The specimen 1RR (beams with flexural reinforcement of 1%) exhibited the maximum ductility of 6.9 and 8.2 obtained from the test and the FE model, respectively.

This study showed that the ductility increases as the number of basalt fabric increases to an optimal number which was found to be four. Beyond this optimal number of layers of

basalt fibre fabric, the ductility reduces. This reduction in ductility can be observed in Figures 5.11 for specimen 0.5RR and 5.14 for specimen 0.75RR, where early failure occurred due to the peeling-off of the fabric and concrete cover together in the beams strengthened with eight layers of basalt fabric (see Figure 5.18 for an example). As can be observed from Table 5.7, the optimal number of basalt fabric layers obtained from the FE models and as well as from the tests for beams with all three flexural reinforcement ratios (0.5%, 0.75%, and 1%) is four. Strengthening of these concrete beams with more than four layers of basalt fibre fabric changes the failure mode of the beams from a ductile failure to a brittle and sudden failure.

Figure 5.18: Shear-tension failure of strengthened beam (Hughes, 2018)

The current study found that the ductility of concrete beams strengthened with basalt fibre fabric can increase. However, previous studies showed that the use of carbon and glass fiber fabrics in strengthening reinforced concrete beams for flexure reduces the ductility (Attari et al., 2012; Kachlakev and Mccurry, 2000). This increase in ductility while using basalt fibre fabric is due to the higher rupture tensile strain (higher ductility)

of basalt fibers as compared to the carbon and glass fibers. Rupture strains of basalt fibre fabric used in this study is 2.35%. However, literature review found that rupture strains of carbon and glass fibre fabrics ranged from 0.7% to 1.5% for carbon fibre fabric and from 1.5% to 2% for glass fibre fabric (Attari et al., 2012; Intelligent Sensing for Innovative Solutions Canada, 2007).

Table 5.7: Ductility Indices of the control and strengthened beams obtained from FE model and test

Beam ID	Deflection at yield (mm)	Deflection at ultimate load (mm)	Ductility (FE model)	Ductility (Test)
0.5RR- Control	3.1	32	10.3	11.1
0.5RR-B02	3.1	33	10.6	11.8
0.5RR-B04	5.1	60	11.8	15.9
0.5RR-B06	5.2	35	6.7	N/A
0.5RR-B08	5.2	32	6.2	6.1
0.75RR- Control	4.7	24	5.1	5.2
0.75RR-B02	5.8	52	8.9	8.4
0.75RR-B04	6.2	56	9.0	9.3
0.75RR-B06	6.2	37	6.0	N/A
0.75RR-B08	6.2	34	5.5	6.8
1RR- Control	5.9	29	4.9	2.7
1RR-B02	5.9	35	5.9	N/A
1RR-B04	6.8	56	8.2	6.9
1RR-B06	6.7	33	4.9	5.3

1RR-B08	6.8	29	4.3	5.0

Note: N/A indicates that the data is not available

5.4 Failure modes

To ensure the models are able to make a good representation of the behavior of the test specimens, the failure modes were compared with the failure modes observed in the test specimens. According to the Canadian standard for the design and construction of buildings with fiber-reinforced polymers (CSA, 2012), the modes of failure in a beam section, is determined by the ratio of the internal compressive resistance to the internal tensile resistance of the section. Relationship 5.5 shows the ratio where the left side is the internal compressive resistance and the right side is the internal tensile resistance. The lower of the two internal resistances is the expected failure mode.

$$\alpha_1 \phi_c f'_c b \beta_1 c + \phi_s f_y A'_s > \phi_s f_y A_s + \phi_{FRP} E_{FRP} \varepsilon_{FRP} A_{FRP} \quad (5.5)$$

In above relationship, $Ø_c$, $Ø_s$, and $Ø_{FRP}$ are the resistance factors for concrete, steel, and FRP, f'_c is the compressive strength of concrete, f_y is the yield strength of steel, β_1 is the ratio of the depth of the neutral axis to the depth of the compression block; A'_s, A_s, and A_{FRP} are the cross-sectional area of steel in compression, cross-sectional area of steel in tension, and the cross-sectional area of FRP, respectively; E_{FRP} and ε_{FRP} are the modulus and ultimate strain values of the FRP.

CSA (2012) categorizes failure modes of reinforced concrete beams strengthened with FRP into two: concrete crushing and fiber rupture. Concrete crushing occurs when the concrete in the compressive region reaches its maximum compressive strain which is considered as 0.0035 or 0.35%. The fiber rupture is assumed to occur when the fiber

laminates (fabrics) bonded to the tension face of the concrete beam attains maximum tensile strain of the fibre which varies with the type of fiber used. Steel yielding, although observed in both tests and FE models, is not considered a failure mode because steel possesses a higher ultimate strain values when compared to both concrete and FRP. In this study however, steel yielding is classified as a failure mode as it ensures the ductility of the beams (Grimaldi and Rinaldi, 2004; Intelligent Sensing for Innovative Solutions Canada, 2007). Ductile failure helps in identifying that the design load for the structure has been attained as visible deflections and cracks begin to appear and propagate and thus, avoiding a sudden failure. A preferred (ductile) failure mode for the specimens is initiated by yielding of steel rebars, followed by concrete crushing, and then rupture of the fiber fabrics. A non-preferred (brittle) failure mode is when the beam fails before the yielding of the steel yield or the rupture of the fibers. All the beams in the experimental program experienced the preferred failure mode except two beams and these are specimens 0.5RR-8L and 0.75RR-8L, which failed suddenly before fiber rupture occurred (see Figure 5.18). This sudden failure, known as shear-tension failure, occurred when the concrete substrate along with the basalt fibre fabric in the tension region debonded from the internal steel reinforcement due to high peeling force applied by the fabric to the bottom of the beam. This caused the fibers to pull out at the cross strap. The FE model did not experience this sudden failure. This could be due to the assumption of a perfect bond between the concrete substrate and the steel reinforcement. The assumption of a perfect bond eliminates the occurrence of bond slip and therefore, the loss of the composite action between concrete and steel reinforcement as observed when the shear tension failure occurred in the test did not occur in the FE models. Although the FE

model did not experience the sudden brittle failure, the FE model experienced a reduction in the values of deflection at the ultimate load signifying a reduction in the effectiveness of the strengthening scheme for these beams. The failure modes observed for the FE models are presented in Table 5.8 below.

Table 5.8: Failure mode of the control and strengthened beams

Beam ID	Failure mode (in order of occurrence)
0.5RR- Control	Steel yielding and concrete crushing
0.5RR-B02	Steel yielding, concrete crushing, and fiber rupture
0.5RR-B04	Steel yielding, concrete crushing, and fiber rupture
0.5RR-B08	Steel yielding, concrete crushing, and fiber rupture
0.75RR- Control	Steel yielding and concrete crushing
0.75RR-B02	Steel yielding, concrete crushing, and fiber rupture
0.75RR-B04	Steel yielding, concrete crushing, and fiber rupture
0.75RR-B08	Steel yielding, concrete crushing, and fiber rupture
1RR- Control	Steel yielding and concrete crushing
1RR-B04	Steel yielding, concrete crushing, and fiber rupture
1RR-B06	Steel yielding, concrete crushing, and fiber rupture
1RR-B08	Steel yielding, concrete crushing, and fiber rupture

5.5 Crack patterns

The concrete crack patterns for the test and the FE model at the ultimate load of the beams were analysed and the results are discussed in this section. It is important to study the formation and propagation of cracks in concrete structures as it greatly affects the

integrity of the structure. Proper modelling of the initiation and propagation of the cracks using finite element method is vital for predicting its behavior. The cracking patterns for the control and strengthened beams were obtained from the FE model which were developed using the damage parameters obtained from the material tests: compression cyclic and wedge-splitting test. The damage parameters help to depict the initiation and propagation of cracks in the beams. The crack patterns of the model were then compared with patterns obtained from the test. Figures 5.19–5.21 show the crack patterns obtained from the test and the FE model of control beam 0.5RR control and strengthened beams 0.5RR-2L and 0.5RR-4L.

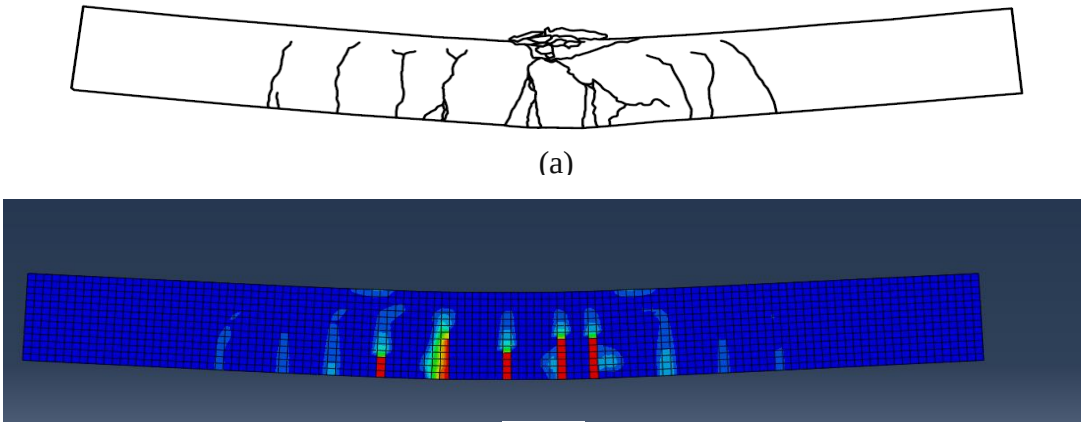

(a)

(b)

Figure 5.19: Crack patterns of control beam 0.5RR (a) Test (Hughes, 2018) (b) FE model

(a)

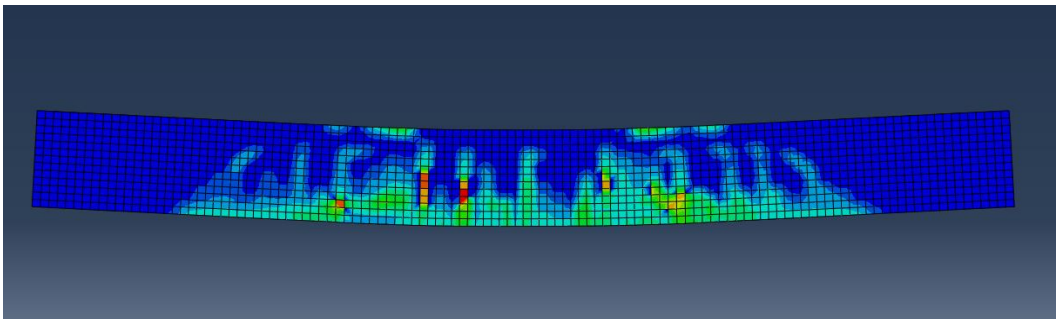

(b)

Figure 5.20: Crack patterns of strengthened beam 0.5RR-2L (a) Test (Hughes, 2018) (b) FE model

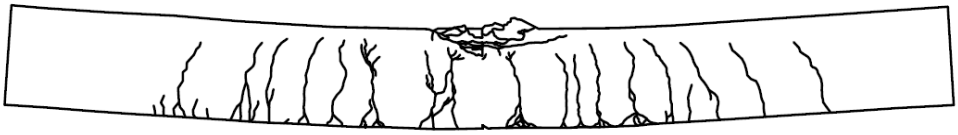

(a)

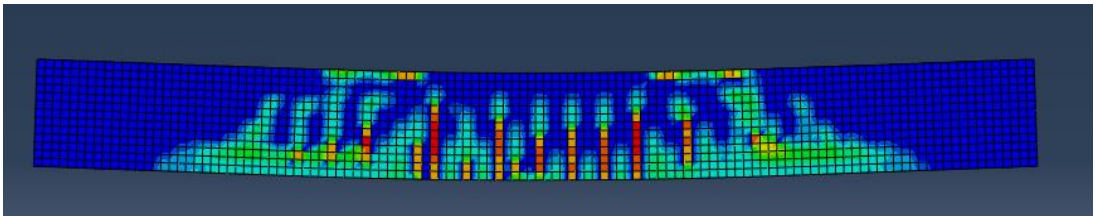

(b)

Figure 5.21: Crack patterns of strengthened beam 0.5RR-4L (a) Test (Hughes, 2018) (b) FE model

As can be found in the Figures 5.19-5.21, the crack patterns of the FE models show a good correlation with those obtained from the test specimens for both the control and strengthened beams with flexural reinforcement ratio of 0.5% (see appendix for the crack patterns of other strengthened beams). Both FE models and test specimens show that the strengthened beams developed a higher number of cracks at failure than the corresponding unstrengthened beams. This could be attributed to the restraining force applied to the beam by the BFRP fabrics attached on the tension face of the beam. This restraining force results in an increase in the strain on the concrete, subsequently increasing the cracks formed on the tension side of the beam.

5.6 Comparison with design codes

In addition to the development of the FE models, the ultimate strength of the beams obtained from the FE models were compared to the results obtained using the Canadian Design and Construction of Building Structures with Fiber-Reinforced Polymers standard (CSA, 2012) and the American Concrete Institute guide for Design and Construction of Externally Bonded FRP Systems for Strengthening Concrete Structures [ACI440.2R-17] (ACI 440, 2017). The calculation of the moment resistance of the concrete beams using these standard and guides is based on the value of the maximum allowable strain of the FRP. While CSA (2012) limits the maximum allowable strain of the FRP to 0.7%. However, ACI440.2R-17 (ACI 2017) allows 90% of the ultimate strain of the FRP. The approach of the ACI guide is better suited for use with basalt fiber fabrics for strengthening of beam since basalt fibre fabric used in this study has a very high ultimate strain of 2.35%. Hence, the recommendation of ACI 440.2R was adopted for the comparison. Equation 5.6 was used to calculate the moment resistance of beams

strengthened with FRP using ACI (2017). The results of the moment resistance using the strain value obtained from ACI guide is compared to those obtained from the FE model and presented in Table 5.9.

$$M_R = C_s\left(\frac{a}{2} - d'\right) + T_s\left(d - \frac{a}{2}\right) + T_{FRP}\left(h - \frac{a}{2}\right) \quad (5.6)$$

In Equation 5.6, M_R is the moment resistance of the beam, C_S is compressive force in steel, T_S is tension force in steel, T_{FRP} is the tension force in the FRP, d′ is distance from the top compression fibre to the centroid of the compressive steel (cover of compression rebar), d and h are the effective depth and height of the beam, respectively and a is the depth of stress block.

Table 5.9: Ultimate strength of the beams

Beam ID	Moment Resistance M_R (kN-m)			
	ACI 440.2R	Test	FE model	% difference
0.5RR-B02	24.9	33.7	31.5	-6.5%
0.5RR-B04	29.8	44.1	42.8	-2.9%
0.5RR-B08	36.6	49.7	51.6	3.8%
0.75RR-B02	28.7	39.9	37.5	-6.0%
0.75RR-B04	36.5	41.0	43.1	5.1%
0.75RR-B08	42.8	59.1	54.9	-7.1%
1RR-B04	42.9	43.8	45.2	3.2%
1RR-B06	43.3	53.5	50.7	-5.2%
1RR-B08	45.7	56.3	54.9	-2.5%

Note: Negative sign means that the FE model predicted a lower value than the test.

Table 5.9 indicates that the ACI 440.2R guide is conservative compared to the both the test specimens and FE models. This is due to the presence of strength reduction factors (material resistance factors) used in limit state design. Nonetheless, the results of the FE models are in good agreement with the results obtained from the test specimens.

5.7 Parametric study

After the successful validation of the FE models, a parametric study was undertaken. The number of basalt fibre fabric was varied as the amount of flexural steel area (flexural steel reinforcement ratio) was kept unchanged. This was done for the three reinforcement ratios (0.5, 0.7, and 1.0) to determine the effect of the increasing the number of layers of basalt fibre fabric on the ultimate load capacity of the concrete beams strengthened for flexure. Figures 5.22 to 5.24 present the results obtained from the parametric study.

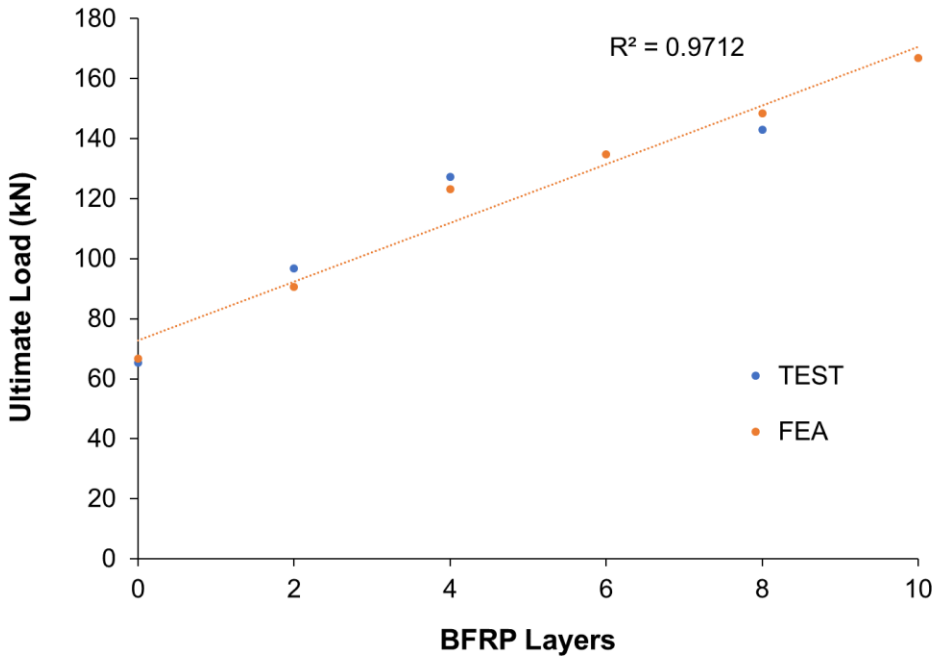

Figure 5.22: Strengthened beams with reinforcement ratio of 0.5%

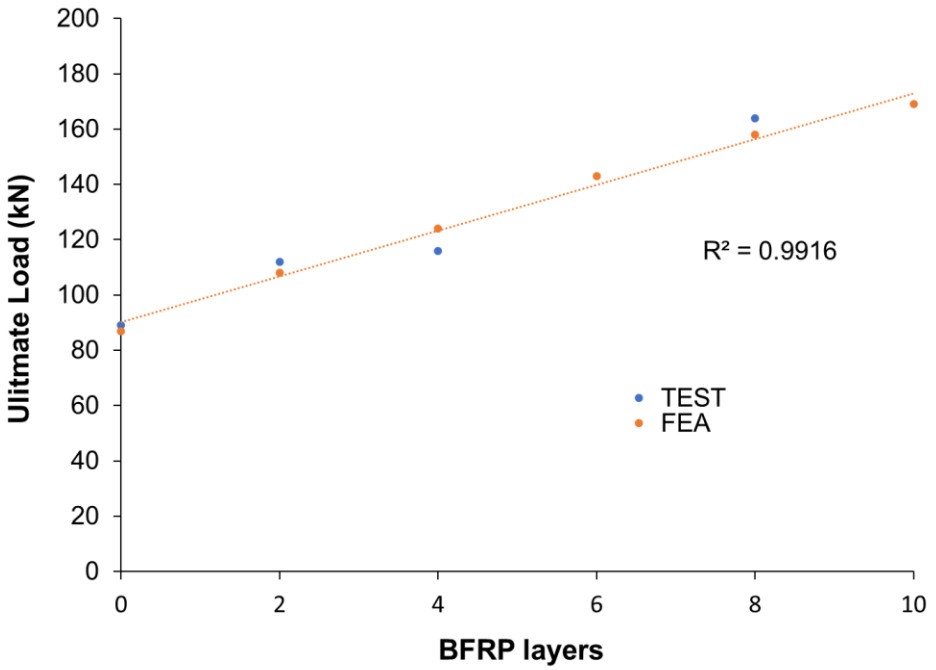

Figure 5.23: Strengthened beams with reinforcement ratio of 0.75%

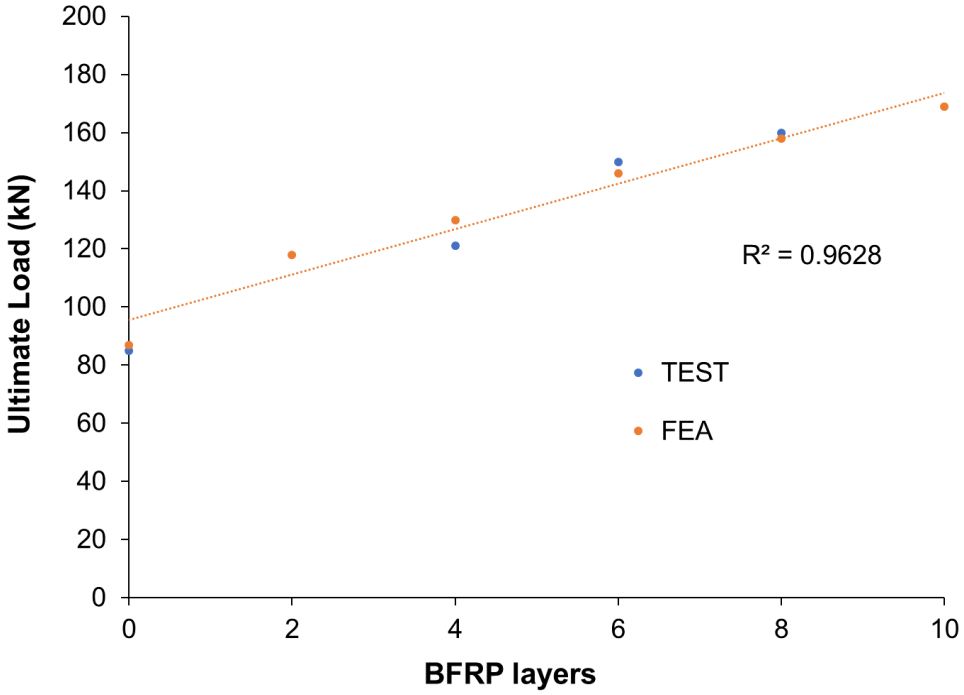

Figure 5.24: Strengthened beams with reinforcement ratio of 1%

For the beams with flexural reinforcement ratio of 0.5%, the R^2 value is 0.9712; whereas, for beams with flexural reinforcement ratio of 0.75% the value of R^2 was found to be 0.9916. For beams with flexural reinforcement ratio of 1%, the R^2 value was 0.9628. These R^2 indicate a good fit for each of the data sets. As discussed earlier in section 5.3 and Table 5.7, the study also showed that when a beam is strengthened with more than four layers (optimum number of layers) of basalt fibre fabric, the ductility of the strengthened beam reduces though the ultimate load capacity increases.

CHAPTER 6
CONCLUSIONS AND RECOMMENDATIONS

6.1 Conclusions

The purpose of this research was to successfully simulate the behavior of reinforced concrete beams and the behavior of reinforced concrete beams externally strengthened with basalt fibre fabric using finite element (FE) method. Three different material tests were conducted to develop 15 FE models using commercially available program, Abaqus. The following conclusions are made based on the outcomes of this study.

1. Flexural strengthening of reinforced concrete beams using basalt fibre fabric was found to be effective in improving the ultimate load capacity and moment resistance of the reinforced concrete beams.
2. Unlike strengthening schemes using carbon and glass fiber fabrics which reduce the ductility of concrete beams, the use of basalt fiber fabric for strengthening however, increases the ductility of the reinforced concrete beams. The increase in the ductility of concrete beams strengthened using basalt fibre fabric ranged from 3.8% to 67% (see Table 5.7) when compared to the ductility of unstrengthened (control) reinforced concrete beam.
3. The FE models developed in this study were successful in predicting the behavior of strengthened and unstrengthened reinforced concrete beams as there was a good correlation between the FE models and the test results.
4. The crack patterns at failure and the failure modes of FE models showed a good correlation with those obtained from the test specimens showing that the damage properties used in the FE model are reasonably accurate.

5. The use of fracture energy as a material property of concrete in tension was found to be effective in simulating the behavior of the beams subjected to flexural loading.
6. The study found the optimum number of layers of basalt fibre fabric required to provide an increased flexural capacity as well as increased ductility for reinforced concrete beams as four. Exceeding this optimum number of basalt fibre fabric layers results in an increase in strength but causes a reduction in the ductility and leads to a brittle failure.

6.2 Recommendations

The following recommendations can be considered when modelling reinforced concrete beams externally strengthened with basalt fibers:

1. Wedge split and cyclic compressive tests are reliable in providing the tensile damage parameters of concrete.
2. Modeling the bond-slip behavior between the concrete and the steel may help to reduce the stiffness of the model and improve the limitation of the model in predicting the shear-tension failure mode observed in the experiment.

REFERENCES

Abaqus. (2018). *Abaqus 6.14 Documentation*. Rising Sun Mills, Providence, RI, USA: Dassault Systèmes Simulia Corp.

Abed, F., & Alhafiz, A. R. (2018). Finite element simulation of the flexural behavior of BFRP-FRC beams. *2018 Advances in Science and Engineering Technology International Conferences, ASET 2018*, 1–5. https://doi.org/10.1109/ICASET.2018.8376768

ACI 446.3R-97. (1997). Finite Element Analysis of Fracture in Concrete Structures: State-of-the-Art. *ACI Committee*, pp33. *American Concrete Institute*. Farmington Hills, MI 48331.

ACI Committee 440. (2017). ACI 440.2R-17: Guide for the design and construction of externally bonded FRP systems for strengthening existing structures. In American Concrete Institute (Ed.), *American Concrete Institute*. Farmington Hills, MI 48331.

Alim, H., Jamil, M., Zisan, M., & Alam, M. (2013). Re-strengthening Of R.C. Beam by Beam Jacketing. *Malaysian Journal of Civil Engineering*, *25*, 119–127.

American Society Of Civil Engineers (ASCE). (2017). Bridge Infrastructure | Structurally Deficient Bridges | ASCE's 2017 Infrastructure Report Card.

Aresh, B., Daadbin, A., & Sarwar, M. (2010). Investigation Into Rock Mechanics Using Finite Element Method. *Asian Rock Mechanicss*, (May). Retrieved from https://www.onepetro.org/conference-paper/ISRM-ARMS6-2010-023

ASTM. (2017a). ASTM C496/C496M-17 Standard Test Method for Splitting Tensile Strength of Cylindrical Concrete Specimens. *American Society for Testing and*

Materials, (October), 1–5. https://doi.org/10.1520/C0496. ASTM International, West Conshohocken, Pennsylvania, USA, 2017.

ASTM. (2017b). ASTM D3039/D3039M Standard Test Method for Tensile Properties of Polymer Matrix Composite Materials1. *American Society for Testing and Materials*, (October), 1–13. https://doi.org/10.1520/D3039. ASTM International, West Conshohocken, Pennsylvania, USA, 2017.

ASTM. (2018a). ASTM A370-18 Standard Test Methods and Definitions for Mechanical Testing of Steel Products. *ASTM Standard*, (October), 1–54. https://doi.org/10.1520/A0370-15.2. ASTM International, West Conshohocken, Pennsylvania, USA, 2018.

ASTM. (2018b). C39/C39M-18: Standard Test Method for Compressive Strength of Cylindrical Concrete Specimens. *American Society for Testing and Materials*, (January), 1–7. https://doi.org/10.1520/C0039. ASTM International, West Conshohocken, Pennsylvania, USA, 2018.

Attari, N., Amziane, S., & Chemrouk, M. (2012). Flexural strengthening of concrete beams using CFRP, GFRP and hybrid FRP sheets. *Construction and Building Materials*. https://doi.org/10.1016/j.conbuildmat.2012.07.052

Blanks, R. F., & Mcnamara, C. C. (1935). Mass concrete tests in large cylinders. *Journal of American Concrete Institute*, (31), 280–303.

Carneiro, F. L., & Barcellos, A. (1949). Tensile strength of concrete. *RILEM Bulletin*, *13*, 98–125.

Cervantes, I., AungYong, L., Chan, K., Ko, Y.-F., & Mendez, S. (2014). Flexural Retrofitting of Reinforced Concrete Structures Using Green Natural Fiber Reinforced Polymer Plates. *Creating Infrastructure for a Sustainianble World*, 1051–1062. https://doi.org/10.1061/9780784478745.099

Chen, G. M., Chen, J. F., & Teng, J. G. (2010). On the finite element modelling of RC beams shear-strengthened with FRP. *Construction and Building Materials*, *32*, 13–26. https://doi.org/10.1016/j.conbuildmat.2010.11.101

Chowdhury, M. R. (1995). Further Considerations for Nonlinear Finite-Element Analysis. *Journal of Structural Engineering*, *121*, 1377–1379.

CIRC. (2019). *Canada Infrastructure Report Card 2019*. Retrieved from http://canadianinfrastructure.ca/en/about.html

Coronado, C. A., & Lopez, M. M. (2006). Sensitivity analysis of reinforced concrete beams strengthened with FRP laminates. *Cement and Concrete Composites*, *28*(1), 102–114. https://doi.org/10.1016/j.cemconcomp.2005.07.005

CSA. (2012). Design and Construction of Building structures with Fibre-Reinforced Polymer. In *CSA S806-12*. Missisauga, Ontario, Canada.

CSA. (2014). *CSA A23.3-14 Design of Concrete Structures*. Missisauga, Ontario, Canada: CSA Group.

DIANA. (2017). Diana User's Manual, Release 10.2. *DIANA FEA BV*. https://doi.org/10.1080/15421400600788682

Earij, A., Alfano, G., Cashell, K., & Zhou, X. (2017). Nonlinear three–dimensional

finite–element modelling of reinforced–concrete beams: Computational challenges and experimental validation. *Engineering Failure Analysis*, *82*(August), 92–115. https://doi.org/10.1016/j.engfailanal.2017.08.025

Einde, L. Van Den, Zhao, L., & Seible, F. (2003). Use of FRP composites in civil structural applications. *Construction and Building Materials*. https://doi.org/10.1016/S0950-0618(03)00040-0

FHWA. (2019). *Tension Testing of Ultra-High Performance Concrete FWHA-HRT-17-053*. (February), 210.

Fiore, V., Scalici, T., Di Bella, G., & Valenza, A. (2015). A review on basalt fibre and its composites. *Composites Part B: Engineering*, *74*, 74–94. https://doi.org/10.1016/j.compositesb.2014.12.034

Głodkowska, W., & Ruchwa, M. (2010). Static Analysis of Reinforced Concrete Beams Strengthened with CFRP Composites/ Analiza Statyczna Belek Zelbetowych Wzmocnionych Tasmami Kompozytowymi. *Archives of Civil Engineering*, *56*(2), 111–122. https://doi.org/10.2478/v.10169-010-0006-9

Graybeal, B. A., & Baby, F. (2014). *Development of Direct Tension Test Method for Ultra-High- Performance Fiber-Reinforced Concrete*. (110), 177–186.

Grimaldi, A., & Rinaldi, Z. (2004). Influence of the steel properties on the ductility of R.C. structures. *Lecture Notes in Applied and Computational Mechanics*, *14*, 297–309. https://doi.org/10.1007/978-3-540-45287-4

Hashin, Z. (1980). Failure Criteria for Unidirectional Fibre Composites. *Journal of*

Applied Mechanics, *47*(2), 329–334. https://doi.org/https://doi.org/10.1007/BF02486267

Hawileh, R. A., Naser, M. Z., & Abdalla, J. A. (2013). Finite element simulation of reinforced concrete beams externally strengthened with short-length CFRP plates. *Composites Part B: Engineering*, *45*(1), 1722–1730. https://doi.org/10.1016/j.compositesb.2012.09.032

Hillerborg, A., Modéer, M., & Petersson, P. E. (1976). Analysis of crack formation and crack growth in concrete by means of fracture mechanics and finite elements. *Cement and Concrete Research*. https://doi.org/10.1016/0008-8846(76)90007-7

Hsu, L. S., & Hsu, C.-T. T. (2009). Complete stress — strain behaviour of high-strength concrete under compression. *Magazine of Concrete Research*, *46*(169), 301–312. https://doi.org/10.1680/macr.1994.46.169.301

Hughes, E. (2018). *Flexural Strengthening Of Reinforced Concrete with Basalt Fibre Reinforced Polymers*. University of Windsor, Windsor ON.

Ibrahim, A. M., & Mahmood, M. S. (2009). Finite element modeling of reinforced concrete beams strengthened with FRP laminates. *European Journal of Scientific Research*, *30*(4), 526–541. Retrieved from http://ieeexplore.ieee.org

Indiamart. (2019). Rehabilitation or structural repairing work. Retrieved May 9, 2019, from https://www.indiamart.com/drdconstruction/rehabilitation-or-structural-repairing-work.html.

Intelligent Sensing for Innovative Solutions Canada. (2007). Reinforcing Concrete

Structures with Fibre Reinforced Polymers. In *(Design Manual No. 3). Reinforcing Concrete Structures with Fibre Reinforced Polymers DESIGN*. Winnipeg, MA, Canada.

Jayasuriya, S., Bastani, A., Kenno, S., Bolisetti, T., & Das, S. (2018). Rehabilitation of Corroded Steel Beams Using BFRP Fabric. *Structures*, *15*(June), 152–161. https://doi.org/10.1016/j.istruc.2018.06.006

Kachlakev, D., & Mccurry, D. D. (2000). *Behavior of full-scale reinforced concrete beams retrofitted for shear and flexure with FRP laminates*. *31*, 445–452.

Kachlakev, D., Niller, T., Yim, S., Chansawat, K., & Potisuk, T. (2001). Finite Element Modeling of Reinforced Concrete Structures Strengthened with FRP Lamiantes. In *Journal of Engineering Materials and Technology*. https://doi.org/10.1121/1.3531810

Kotsovos, M. D., & Newman, J. . (1981). Fracture mechanics and concrete behaviour. *Magazine of Concrete Research*, *33*(115), 103–112.

Lee, J., & Fenves, G. L. (1998). Plastic-Damage Model for Cyclic Loading of Concrete Structures. *Journal of Engineering Mechanics*, *124*, 892–900.

Lihua, H., Yujing, L., & Yuefang, W. (2013). Strenghtening effects of BFRP on reinforced concrete beams. *Journal of Southeast University*, *29*(2), 182–186. https://doi.org/10.3969/j.issn.1003-7985.2013.02.013

Lubliner, J., Oliver, J., Oller, S., & Oñate, E. (1989). A plastic-damage model for concrete. *International Journal of Solids and Structures*.

https://doi.org/10.1016/0020-7683(89)90050-4

MATLAB. (2014). Matlab documentation. *The Mathworks Inc.* https://doi.org/10.1201/9781420034950

Michał, S., & Andrzej, W. (2015). Calibration of the CDP model parameters in Abaqus. *The 2015 World Congress on Advances in Structural Engineering and Mechanics*, 25–29. Retrieved from http://www.i-asem.org/publication_conf/asem15/3.CTCS15/1w/W1D.1.AWinnicki.CAC.pdf

Nayal, R., & Rasheed, H. A. (2006). Tension Stiffening Model for Concrete Beams Reinforced with Steel and FRP Bars. *Journal of Materials in Civil Engineering*, *18*(6), 831–841. https://doi.org/10.1061/(asce)0899-1561(2006)18:6(831)

Nie, J., Wang, Y., & Cai, C. S. (2010). Experimental Research on Fatigue Behavior of RC Beams Strengthened with Steel Plate-Concrete Composite Technique. *Journal of Structural Engineering*. https://doi.org/10.1061/(asce)st.1943-541x.0000336

Nikishkov, G. P. (2004). *Introduction to the Finite Element Method* (p. 45). p. 45. https://doi.org/10.7142/igakutoshokan.55.211

Nilson, A. H., & Winter, G. (1991). *Design of Concrete Structures* (10th ed.). New York: McGraw Hill.

Obaidat, Y. T., Heyden, S., & Dahlblom, O. (2010). The effect of CFRP and CFRP/concrete interface models when modelling retrofitted RC beams with FEM. *Composite Structures*, *92*(6), 1391–1398. https://doi.org/10.1016/j.compstruct.2009.11.008

Østergaard, L., Damkilde, L., & Stang, H. (2003). *Early age fracture mechanics and cracking of concrete: Experiments and Modelling*. Denmark.

Parashar, S. K., & Sharma, J. K. (2016). A review on application of finite element modelling in bone biomechanics. *Perspectives in Science*, *8*, 696–698. https://doi.org/10.1016/j.pisc.2016.06.062

Pham, H., & Al-Mahaidi, R. (2005). Finite element modelling of RC beams retrofitted with CFRP fabrics. *ACI Special Publication*, (January 2005), 499–514. Retrieved from http://www.concrete.org/Publications/InternationalConcreteAbstractsPortal.aspx

Rabbat, B. G., & Russell, H. G. (1985). Friction coefficient of steel on concrete or grout. *Journal of Structural Engineering (United States)*, *111*(3), 505–515. https://doi.org/10.1061/(ASCE)0733-9445(1985)111:3(505)

Radfar, S. (Laboratoire N., Foret, G. (Laboratoire N., & Sab, K. (Laboratoire N. (2012). *Failure Mode Analyses of Fiber Reinforced Polymer plated Reinfroced Concrete Beams*. 1–8. Retrieved from https://pdfs.semanticscholar.org

Rao, G. A., Vijayanand, I., & Eligehausen, R. (2007). Studies on ductility of RC beams in flexure and size effect. *Proceedings of the 6th International Conference on Fracture Mechanics of Concrete and Concrete Structures*, *2*, 671–675.

RILEM Technical committee 50-FMC. (1985). Determination of the Fracture Energy of Mortar and Concrete by Means of Three-point Bend Tests on Notched Beams. *Materials and Structures*, *106*, 285–290.

Saadatmanesh, H., & Ehsani, M. R. (2007). RC Beams Strengthened with GFRP Plates. I: Experimental Study. *Journal of Structural Engineering*. https://doi.org/10.1061/(asce)0733-9445(1991)117:11(3417)

Sagher, A., & Abed, F. (2017). Finite element parametric study of the shear behavior of GFRP-RC short beams. *2017 7th International Conference on Modeling, Simulation, and Applied Optimization, ICMSAO 2017*, 1–5. https://doi.org/10.1109/ICMSAO.2017.7934912

Said, M., Adam, M. A., Mahmoud, A. A., & Shanour, A. S. (2016). Experimental and analytical shear evaluation of concrete beams reinforced with glass fiber reinforced polymers bars. *Construction and Building Materials*, *102*(3), 574–591. https://doi.org/10.1016/j.conbuildmat.2015.10.185

Sim, J., Park, C., & Moon, D. Y. (2005). Characteristics of basalt fiber as a strengthening material for concrete structures. *Composites Part B: Engineering*, *36*(6–7), 504–512. https://doi.org/10.1016/j.compositesb.2005.02.002

Sousa, J. L. A. de O. e, & Gettu, R. (2006). Determining the tensile stress-crack opening curve of concrete by inverse analysis. *Journal of Engineering Mechanics*, *132*(2), 141–148. https://doi.org/10.1061/(ASCE)0733-9399(2006)132:2(141)

Timoshenko, S., & Goodier, J. . (1970). Thoery of Elasticity.

Tomlinson, D., & Fam, A. (2015). Performance of Concrete Beams Reinforced with Basalt FRP for Flexure and Shear. *Journal of Composites for Construction*, *19*(2), 1–10. https://doi.org/10.1061/(ASCE)CC.1943-5614.0000491.

Uday, N. P. (2017). *Experimental Determination of Fracture Energy by RILEM Method*. (June 2015), 106–115. https://doi.org/10.9790/1813-060301106115

Wahalathantri, B. L., Thambiratnam, D. P., Chan, T. H. T., & Fawzia, S. (2011). A material model for flexural crack simulation in RC using ABAQUS. *First International Conference on Engineering, Designing and Developing the Built Environment for Sustainable Wellbeing*, 260–264. https://doi.org/10.1007/BF02906653

Yuan, F., Pan, J., & Leung, C. K. Y. (2013). Flexural behaviors of ECC and concrete/ECC composite beams reinforced with basalt fiber-reinforced polymer. *Journal of Composites for Construction*, *17*(5), 591–602. https://doi.org/10.1061/(ASCE)CC.1943-5614.0000381

APPENDIX A

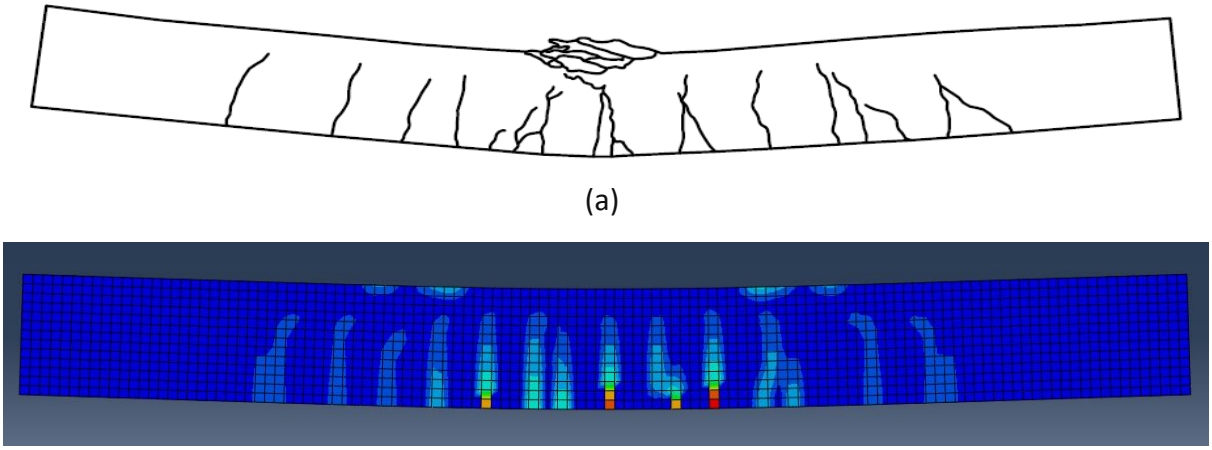

Figure A.1: Crack patterns of control beam 0.75RR (a) Test (b) FE model

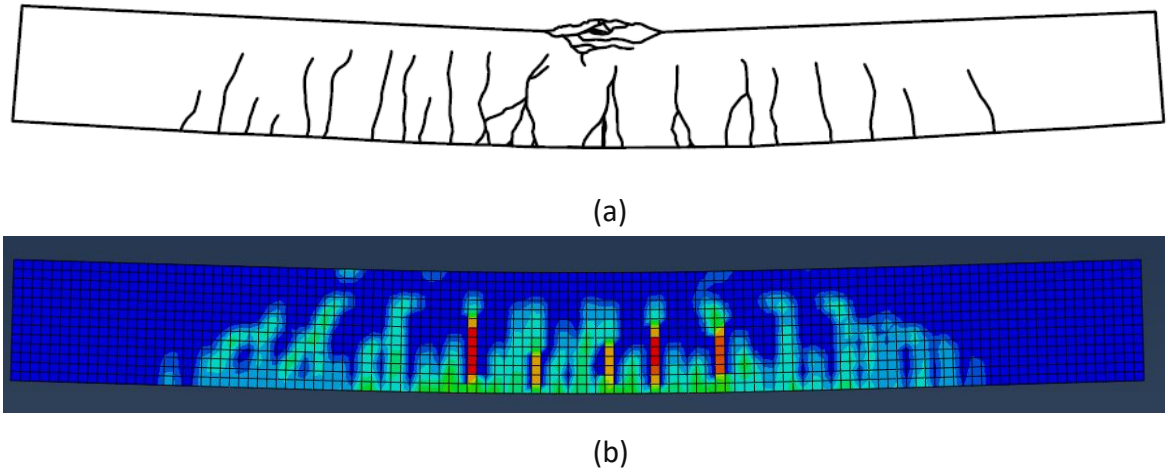

Figure A.2 Crack patterns of strengthened beam 0.75RR-2L (a) Test (b) FE model

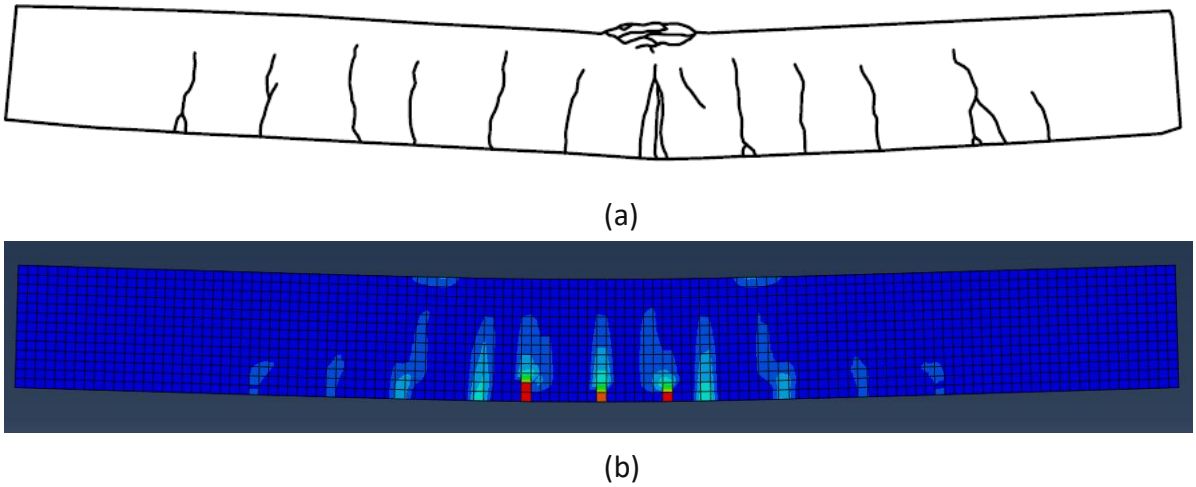

Figure A.3: Crack patterns of control beam 1RR (a) Test (b) FE model

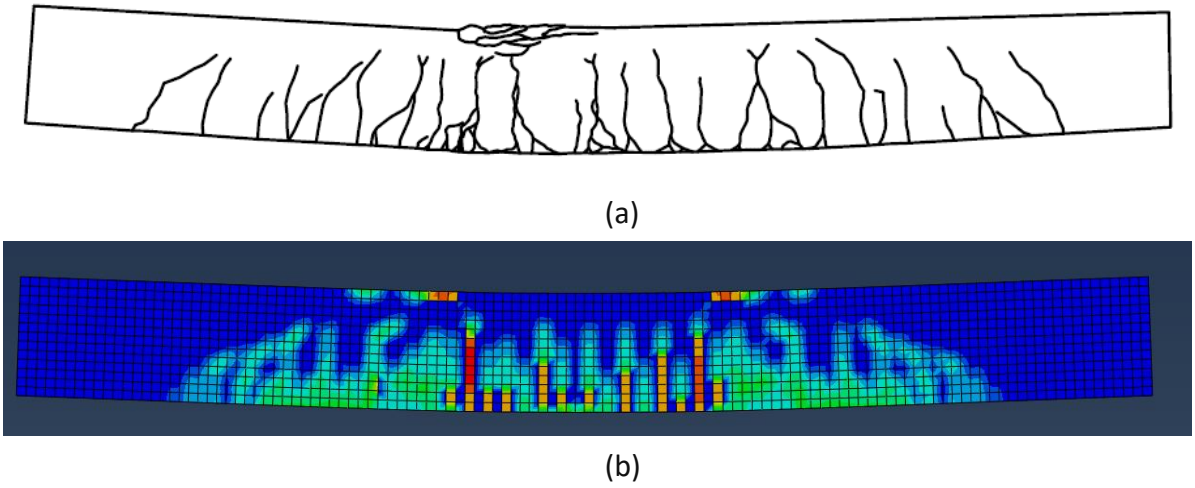

Figure A.4: Crack patterns of strengthened beam 1RR-4L (a) Test (b) FE model

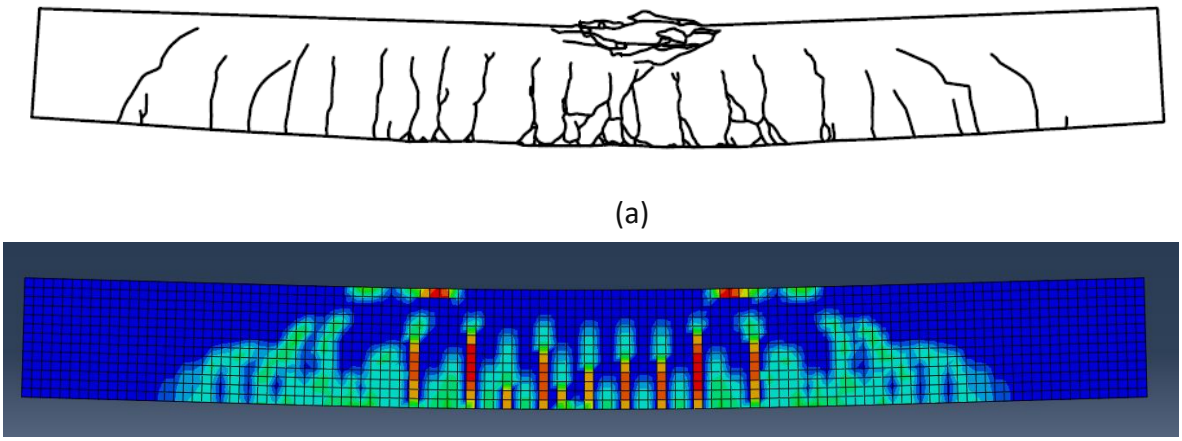

Figure A.5: Crack patterns of strengthened beam 1RR-6L (a) Test (b) FE model

VITA AUCTORIS

NAME:	Iyinoluwa Stephen
PLACE OF BIRTH:	Lagos, Nigeria
YEAR OF BIRTH:	1992
EDUCATION:	Covenant University, B.Sc. – Civil Engineering Ota, Nigeria, 2013
	University of Windsor, M.A.Sc. – Civil Engineering Windsor, ON, 2019